PNAS
www.pnas.org

Supplementary Information for

Microscopic origins of the crystallographically preferred growth in evaporation-induced colloidal crystals

Ling Li, Carl Goodrich, Haizhao Yang, Katherine R. Phillips, Zian Jia, Hongshun Chen, Lifeng Wang, Jinjin Zhong, Anhua Liu, Jianfeng Lu, Jianwei Shuai, Joanna Aizenberg

Ling Li and Joanna Aizenberg
E-mail: lingl@vt.edu, and jaiz@seas.harvard.edu.

This PDF file includes:

Supplementary Note 1: Numerical simulations for colloidal crystallization
Supplementary Note 2: Continuum analysis of dislocation behavior
Supplementary Figures: Figs. S1-29
Supplementary Movies: Movies S1-4
SI References

Supplementary note 1:
Numerical simulations for colloidal crystallization

We model colloidal crystallization as a collection of microspheres in a three-dimensional simulation box that is periodic only in the M (meniscus) direction. In the N (normal) direction, the colloids are confined by two soft walls, while in the G (growth) direction the crystal is held together through a combination of fixed particles and a constant "hydrodynamic" force as discussed below.

The system is initialized with a pre-formed FCC crystal in a given orientation and lattice spacing that extends only a few layers in the G direction and is held fixed throughout the simulation. Mobile colloids then flow in the $-G$ direction due to the constant hydrodynamic force until they reach the crystal and join at the growing end. The shrinking of the colloids due to their drying is modeled as a gradual decrease in colloid radius after the sphere joins the crystal. As the colloids shrink, there is an induced tension in the M direction due to a short-ranged attractive interaction between the colloids that cannot be trivially relaxed away because of the periodic boundary conditions. This tensile stress field leads to reorganizations of the crystal, including defect-mediated crystallographic rotations. After the particles become sufficiently dry, their position is fixed to prevent unphysical accumulation of the hydrodynamic force.

Brownian dynamics: The dynamics of the microspheres are given by the overdamped Langevin equation:

$$\frac{d\vec{r}_i}{dt} = \frac{1}{\gamma_i}\vec{F}_i + \sqrt{\frac{2k_BT}{\gamma_i}}\vec{f}_i(t)$$

for microsphere i, where γ_i is the friction coefficient, $\vec{F}_i$ is the force on particle i (calculated by taking the gradient of the total energy, see below), k_B is the Boltzmann constant, T is the temperature, and the elements of $\vec{f}_i(t)$ are Gaussian random variables that satisfy $\langle f_i^{\alpha}(t)\rangle = 0$ and $\langle f_i^{\alpha}(t) f_j^{\beta}(t')\rangle = \delta_{ij}\delta_{\alpha\beta}\delta(t-t')$, where α and β index spatial dimensions. The friction coefficient for particle i is given by $\gamma_i = 6\pi\eta R_i$, where η is the dynamic viscosity and R_i is the radius of particle i. The overdamped Langevin equation is integrated numerically using a fixed time step Δt. When a particle is designated as fixed, it does not move regardless of the force. The values of relevant parameters used in the simulation are given in (Supplementary Table. S1).

Potentials: Each colloid experiences the following interactions.

1. Colloid-colloid interactions: For two colloids i and j at positions $\vec{r}_i$ and $\vec{r}_j$ and that have radii R_i and R_j, the interaction between these colloids is given by

$$V(\delta) = \begin{cases} V_h(\delta), & \delta < R_{switch} \\ V_m(\delta), & R_{switch} \le \delta < R_{off} \\ 0, & \delta \ge R_{off} \end{cases}$$

where $\delta = \frac{|\vec{r}_j - \vec{r}_i|}{\sigma_{ij}}$ and $\sigma_{ij} = R_i + R_j$. $V_h(\delta)$ is a harmonic repulsive interaction given by

$$V_h(\delta) = \frac{k}{2}(\delta - \delta_0)^2 + kB\delta + A,$$

and $V_m(\delta)$ is a Morse-like attractive interaction given by

$$V_m(\delta) = \frac{k}{2a^2}\left(e^{-2a(\delta-\delta_0)} - 2e^{-a(\delta-\delta_0)}\right) + kDr + C$$

Supplementary Table S1 | List of parameters for Brownian dynamics simulation.

Brownian dynamics					
Parameter	η	Δt	$k_B T$		
Value	1	0.01	$4.67 * 10^{-6}$		
Interaction potentials					
Parameter	k	δ_0	α	k_{wall}	f_0
Value	10	1	30	100	0.1
Microsphere size					
Parameter	R_{max}	S	t_{start}	t_{end}	t_{fix}
Value	0.185	0.95	0	16000	32000

All masses are measured in units of picograms, distances in units of micrometers, time in units of microseconds, and temperature in Kelvin. All other quantities are given in the appropriate combination of these units.

We choose the normalized cutoff distance to be $R_{off} = \delta_0 + \frac{4}{a}$, while the value of R_{switch} is taken to be the point where $\frac{dV_h(\delta)}{d\delta} = 0$, *i.e.* $R_{switch} = \delta_0 - B$. The values of A, B, C, and D are chosen so that $V(\delta)$ and $\frac{dV(\delta)}{d\delta}$ are continuous at R_{switch} and approach zero at R_{off}. Therefore, $V(\delta)$ is a function with just three remaining parameters: k, δ_0, and α. $V(\delta)$ and the force $F(\delta) = -\frac{dV(\delta)}{d\delta}$ are shown in (Fig. S16).

2. Colloid-wall interactions: We impose two soft confining walls perpendicular to the N direction, a lower wall and an upper wall. A particle with position n in the N direction experiences the following interaction

$$V_{wall}(n) = \frac{k_{wall}}{2}\left[\left(n_{wall,lower} - n\right)^2 \Theta\left(n_{wall,lower} - n\right) + \left(n - n_{wall,upper}\right)^2 \Theta(n - n_{wall,upper})\right],$$

where $n_{wall,lower}$ and $n_{wall,upper}$ are the positions of the two walls and are chosen so as to constrain the crystal to 6 layers.

3. Constant driving force: We approximate the hydrodynamic force on the colloids as a constant force in the $-G$ direction. This can be represented with the following potential applied to every particle:

$$V_{pulling}(g) = f_0 g$$

where g is the position of the particle in the G direction and f_0 is the magnitude of the constant force.

Particle shrinking: To simulate the effects of particle drying, the microspheres in our simulations shrink over time. This shrinking is regulated by measuring the time that each particle joins the crystal, which is defined by when the velocity of the particle drops below a particular threshold. If we define τ to be the time since a particle joins the crystal, the particle's radius is the following function of τ

$$R_i(\tau) = \begin{cases} R_{max}, & \tau < t_{start} \\ \left[1 - (1-S)\dfrac{\tau - t_{start}}{t_{end} - t_{start}}\right] R_{max}, & t_{start} \le \tau < t_{end} \\ SR_{max}, & t \ge t_{end} \end{cases}$$

where $S = R_{min}/R_{max}$ gives the amount that the particle shrinks, and t_{start} and t_{end} give time range over which the shrinking occurs (see Fig. S17). Also shown in Fig. S17, t_{fix} is the time when the particle becomes fixed.

Supplementary note 2:
Continuum analysis of dislocation behavoir

As discussed in the main text, a tensile stress/strain field is generated during the drying process of the assembled colloidal crystal, which is primarily due to the shrinkage of colloidal particles. This tensile stress/strain field is dominated in the meniscus direction (*48,50*). Here we evaluate the accommodation of the drying strain in this direction due to the presence of geometrically necessary dislocations. Following the one-dimensional dislocation model (*9,54,55*), the elastic energy stored in a strained film with a thickness *h* is

$$U_{el} = \frac{1}{2}\varepsilon_{el}^2 Eh$$

per unit area, where *E* is the Young's modulus of the film.

The elastic strain $\varepsilon_{el} = \varepsilon_0 - \varepsilon$ and ε_0 is the total strain due to particle shrinkage during the drying process. ε is the strain relieved by the dislocations, which is given by

$$\varepsilon = b\cos\alpha\Lambda^{-1}$$

where b is magnitude of the Burgers vector of the dislocation, α is the angle beween the Burgers vector and its projection onto the loading direction, and Λ^{-1} represents the number of dislocations per unit length (Λ represents the average spacing between adjacent dislocations).

The energy cost per unit area associated with the dislocations is given as

$$U_L = \frac{\Lambda^{-1}}{4\pi(1-\upsilon)}\mu b^2 \ln\frac{R}{r_c}$$

where υ is Poisson's ratio, μ is shear modulus, R and r_c are the outer and core radii of the strain field associated with the dislocation.

We then have the total energy of the film as

$$\begin{aligned} U_{tot} &= U_{el} + U_L \\ &= \frac{1}{2}\left(\varepsilon_0 - b\cos\alpha\Lambda^{-1}\right)^2 Eh + \frac{\Lambda^{-1}}{4\pi(1-\upsilon)}\mu b^2 \ln\frac{R}{r_c} \end{aligned}$$

Minimizing the total energy with respect of Λ^{-1}, we have

$$\Lambda^{-1} = \frac{\varepsilon_0}{b\cos\alpha} - \frac{\mu}{4\pi E(1-\upsilon)h\cos^2\alpha}\ln\frac{R}{r_c}.$$

A critical thickness h_c exists when Λ^{-1} approaches zero (critical thickness for the generation of dislocations):

$$\Lambda^{-1} = 0 = \frac{\varepsilon_0}{b\cos\alpha} - \frac{\mu}{4\pi E(1-\upsilon)h_c\cos^2\alpha}\ln\frac{R}{r_c}$$

Here, by taking R to be the film thickness ($R = h_c$) (*9*), we have

$$h_c = \frac{\mu b}{4\pi\varepsilon_0 E(1-\upsilon)\cos\alpha}\ln\frac{h_c}{r_c}$$

To estimate h_c , we take ε_0 to be 0.05, and r_c to be b/4 (*9,56,57*). We also have the relation $E/\mu = 2(1+\upsilon)$ for an isotropic elastic material and the Poisson ratio can be assumed as $\upsilon = 1/3$. Here we consider the scenario most favaorable for generating dislocations, i.e., $\theta = 15°$. Note that the loading direction is given by [A, -1, 1-A], where A = $tan(\theta)$, as discussed in the supplementary notes on Schmid factor analysis. In this case, the corresponding partial dislocation Burgers vector is $\frac{1}{6}\left[1\bar{2}\bar{1}\right]$, from which we have $\cos\alpha = 0.4944$. After solving the nonlinear equation, we have $h_c = 1.24$ μm. For an FCC crystal with (111) plane parallel to the substrate, we further have

$$h = \frac{d}{2} + \frac{\sqrt{3}(n-1)d}{2}$$

where n represents the number of layers. For $h_c = 1.24$ μm and d = 0.38 μm, we find n = 4.2 layers. Consistent with this prediction, for regions with the number of layers fewer than five layers, very limited dislocations and hence the crystallographic rotation behavior were observed. In contrast, the dislocations were present for regions with six or more layers, consistent with the prediction.

Supplementary Figures

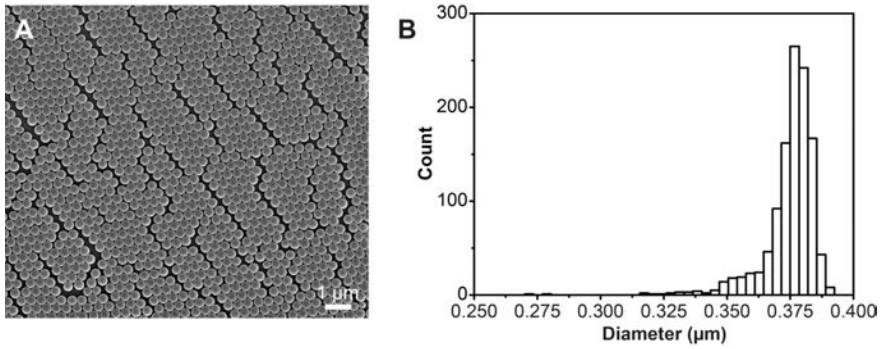

Fig. S1. Size analysis of PS colloids. (**A**) An SEM image of the polystyrene (PS) particles used in this study. (**B**) Size distribution of the PS particles: 375 ± 11 nm (n = 1148, 2.8% polydispersity).

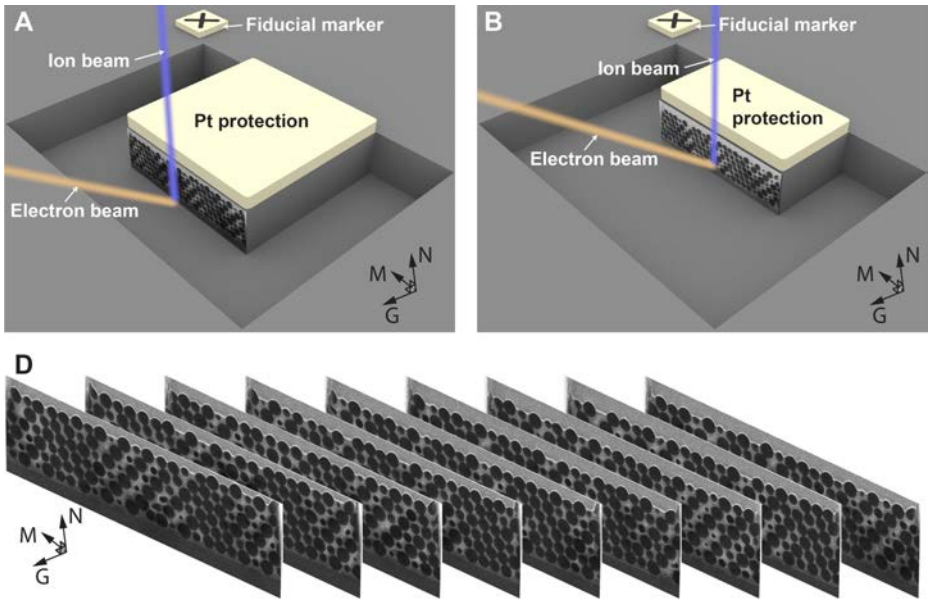

Fig. S2. Schematic diagrams of FIB/SEM-based nanotomography measurement. (**A,B**) The tomography data was generated by sequential milling by using the ion beam and subsequent imaging with the electron beam. (**C**) Schematic view of the image stack along the growth direction (G).

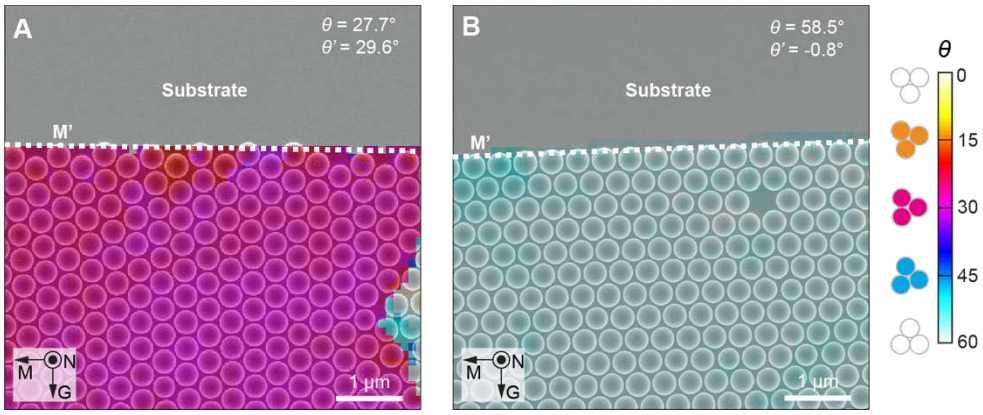

Fig. S3. Representative grains with different values of θ and θ'. (**A,B**) SEM images overlayed with orientation maps, for grains with the close-packed direction (**A**) perpendicular to, and (**B**) along the local meniscus. The white dashed lines (*M'*) indicate the local meniscus orientation.

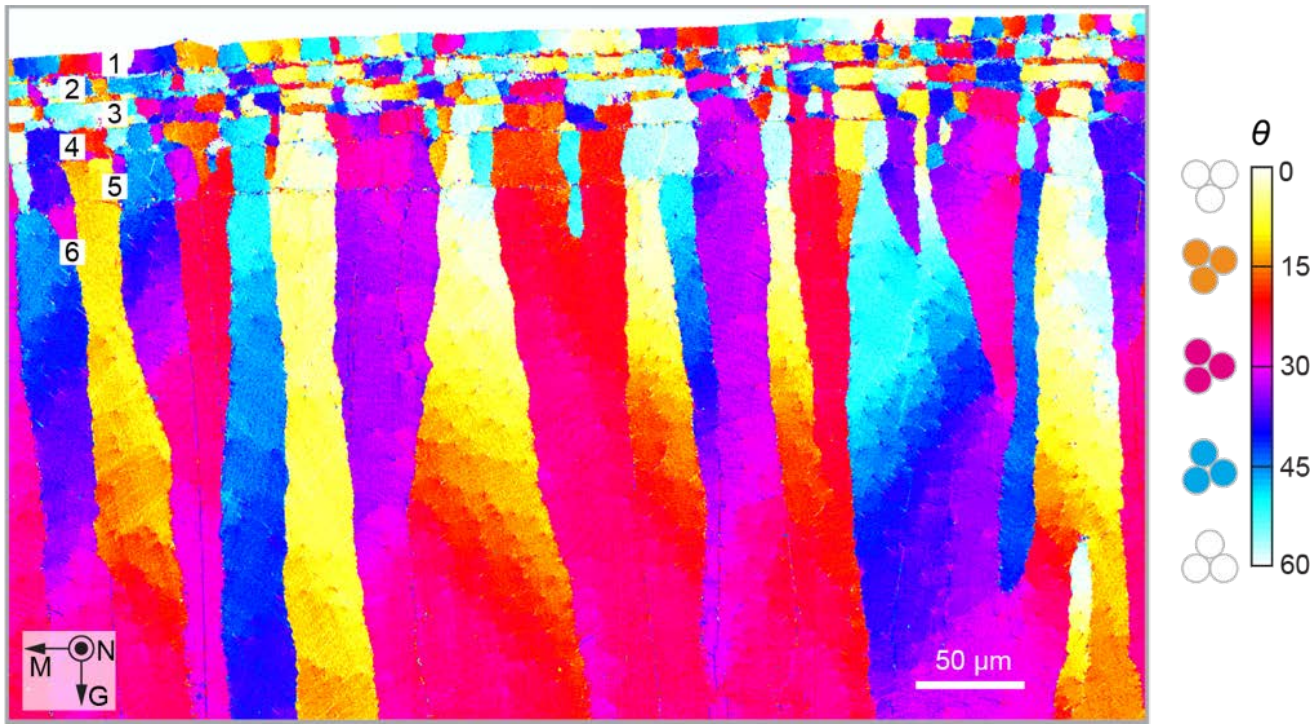

Fig. S4. A large-area grain orientation map close to the growth initiation region. The number of layers increases from 1 to 6 in the first ~70 µm, then remains constant for >200 µm.

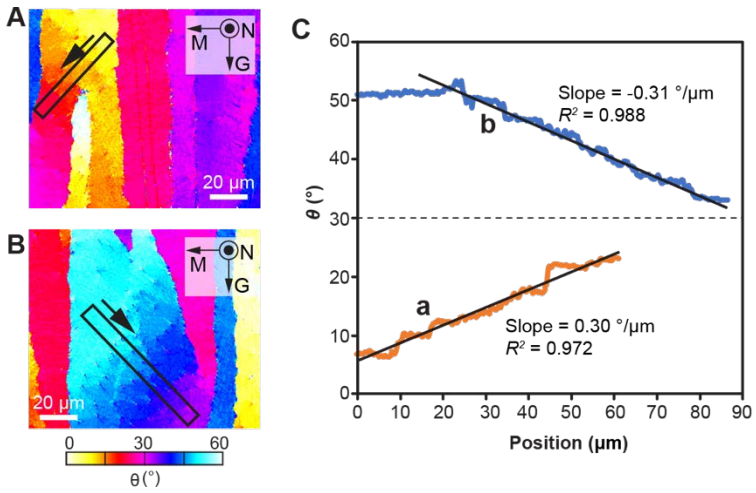

Fig. S5. Analysis of individual grain's crystallographic gradients. (**A,B**) Two representative orientation maps of grains with (**A**) $0° < \theta < 30°$ and (**B**) $30° < \theta < 60°$, respectively. (**C**), The profile of crystal orientation θ as a function of positions, for the regions indicated by the rectangular boxes and the arrows in (**A**) and (**B**). Linear trends observed in both cases indicate an approximately constant rotation of ~0.3°/µm over a distance of more than 50 µm.

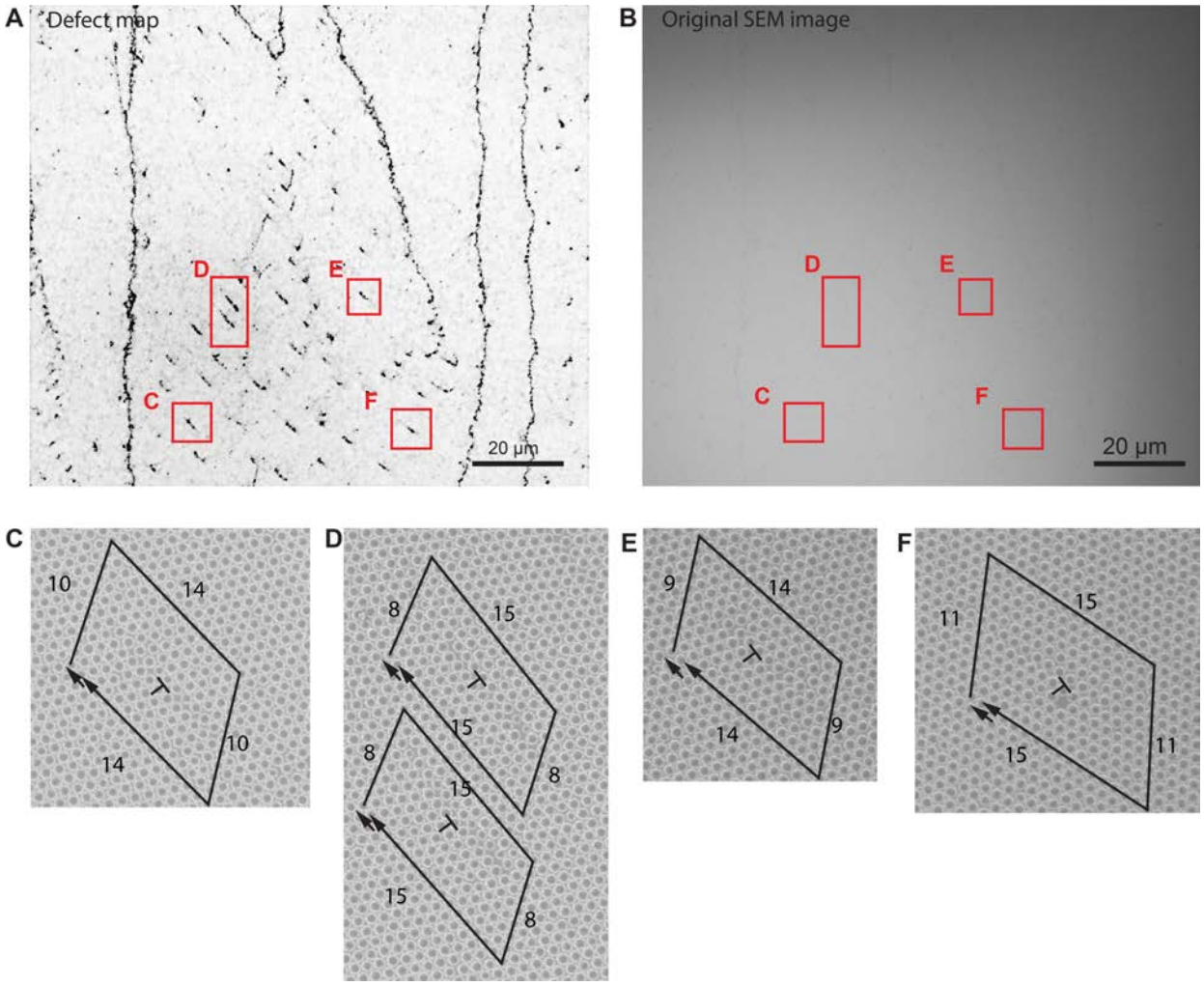

Fig. S6. Demonstration of a/2<110>-type dislocations over large areas. (**A**) Defect map and (**B**) corresponding original SEM image of a representative region. (**C-F**) Random selected dislocations with Burgers circuits labelled. All dislocations exhibit the a/2<110> type.

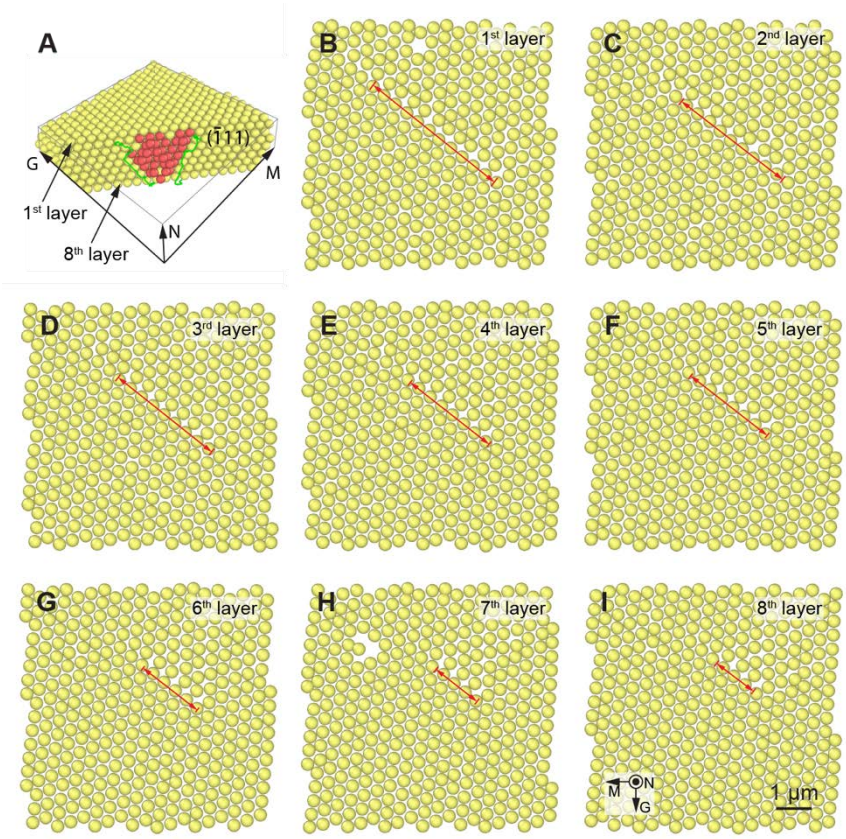

Fig. S7. Visualization of the stacking fault defect in each individual layer of the colloidal crystal. (**A**) Reconstruction of the 8-layer colloidal crystal with a stacking fault (indicated by red particles) embedded in a perfect fcc lattice (yellow particles). (**B-I**) Top-view images of crystal reconstruction for each individual layer. The red lines indicate the location and length of the stacking fault. The first layer is the topmost layer, and the eighth layer is on the substrate.

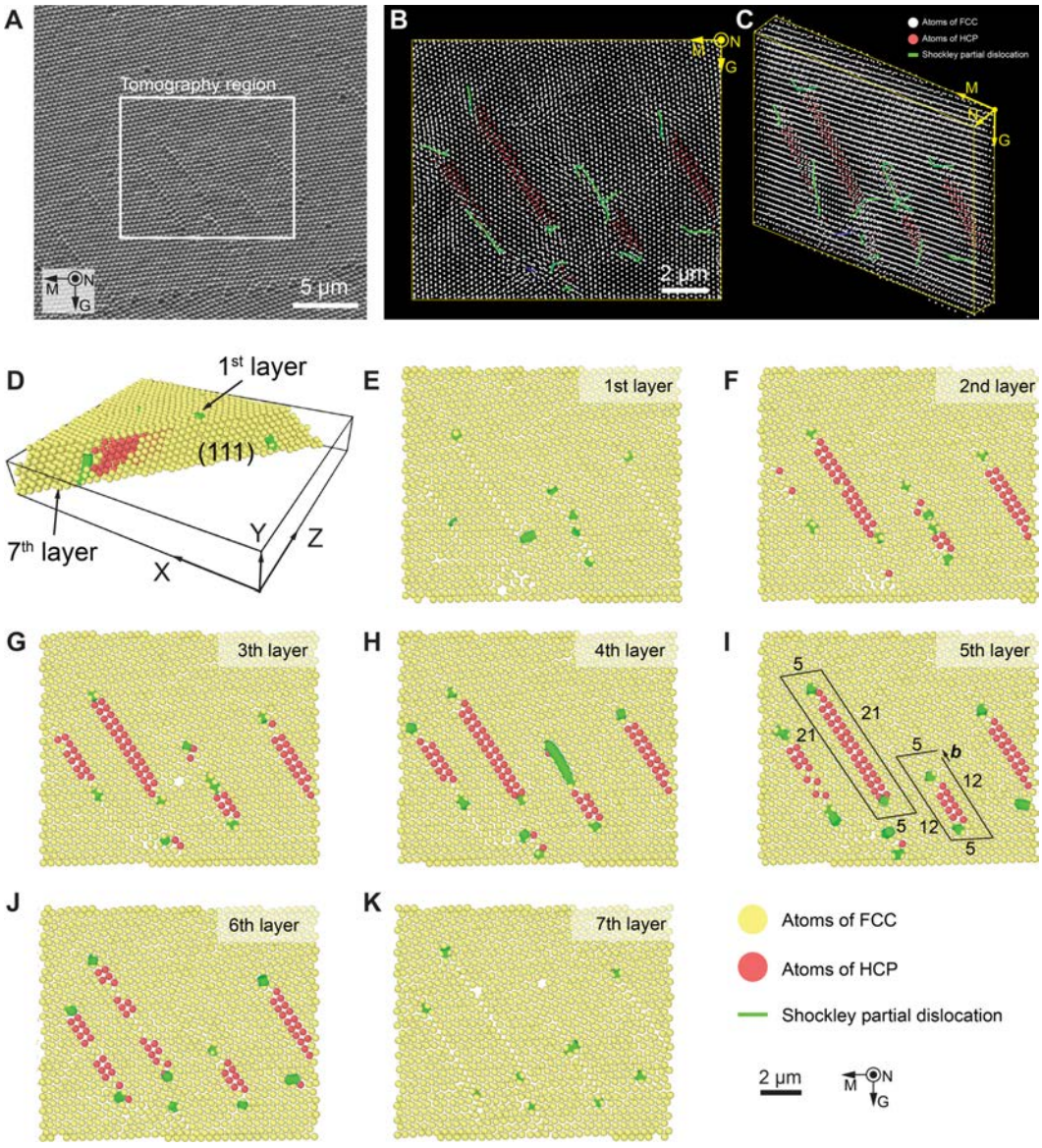

Fig. S8. Tomography analysis of multiple dislocations within a localized region. (**A**) Original SEM image showing the region used for tomography measurement (white box). (**B,C**) 3D view of the colloidal crystal where the positions of individual colloids are identified. The multiple stacking faculty due to the presence of dislocations are highlighted. (**D**) Reconstruction of this 7-layer colloidal crystal, which shows one stacking fault (indicated by red particles) embedded in the perfect fcc lattice (yellow particles). (**E-K**) Top-view images of crystal reconstruction for each individual layer. The red lines indicate the location and length of the stacking fault. The first layer is the topmost layer, and the seventh layer is on the substrate. As shown in (**I**), here in this region, a stacking fault (labeled as "5-21-5-21") is bounded with the partial dislocations with the same Burgers vector of the a/6<112> type, hence, the net Burgers vector is zero. Note that the dominating majoring dislocation type is the one shown in Fig. 3 and Fig. S6 with net non-zero Burgers vecor of the a/2<110> type.

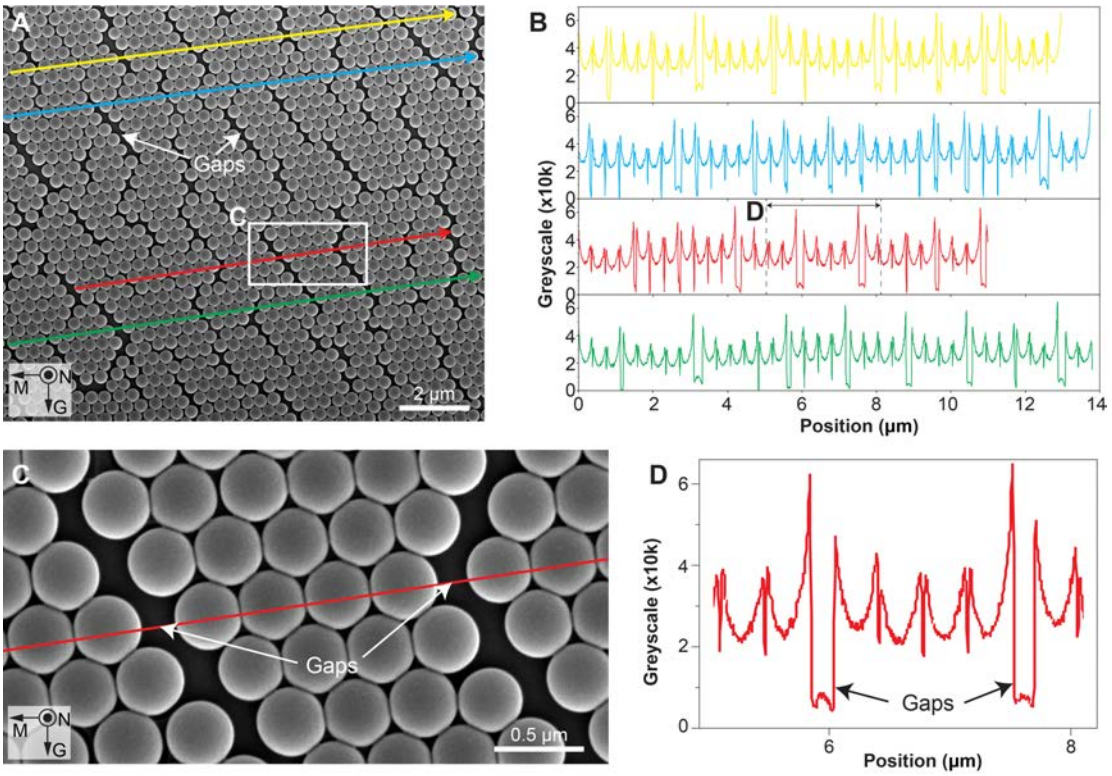

Fig. S9. Estimation of the shrinkage of colloidal particles after drying. (**A**) SEM image of a single layer of PS particles after the assembly was completely dried. Due to the particle shrinkage, crack-like gaps were formed. Note that the cracks follow one of the close-packed directions, which are the least parallel to the meniscus direction. This is due to the fact that the tensile stress generated during the drying process is primarily along the meniscus direction. (**B**) Profiles of the greyscale intensity along four selected directions (shown in (A)). (**C**) A zoom-in view of the gaps and (**D**) corresponding greyscale intensity profile, from which the gap spacing can be calculated. The gap spacing resulted from the drying process is estimated as ca. 5%.

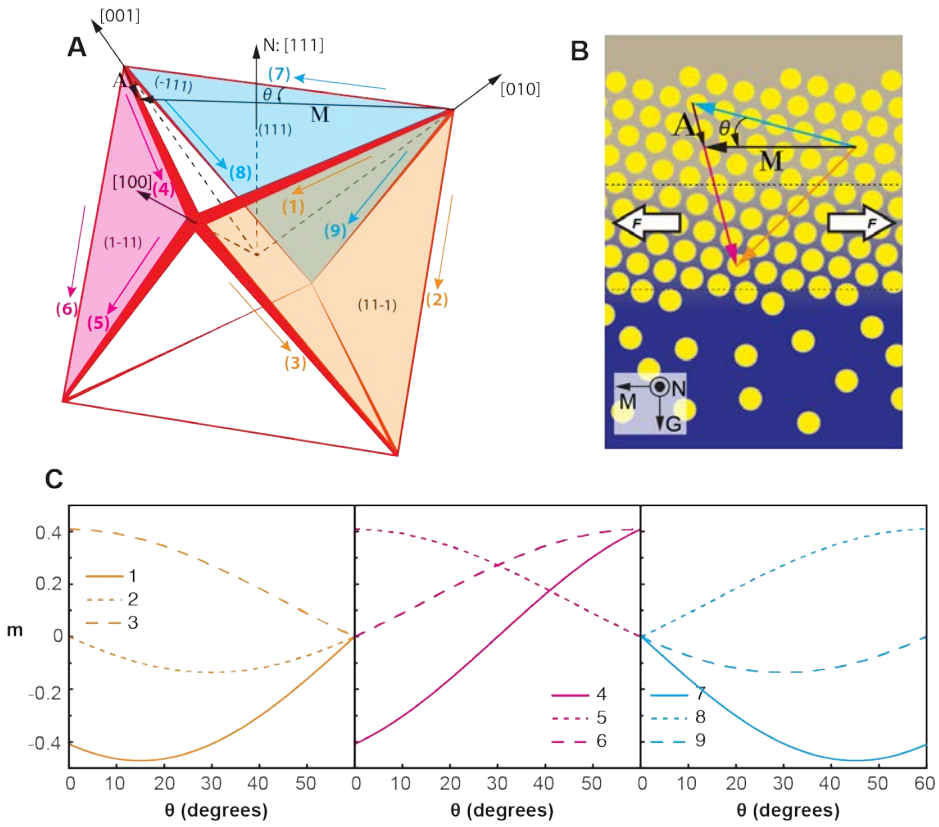

Fig. S10. Schmid factor analysis in all the relevant slip systems. (**A**) A schematic diagram showing the involved three slip planes: $(11\bar{1})$, $(1\bar{1}1)$, and $(\bar{1}11)$. In each slip plane, three slip orientations are also indicated. See the Methods section for further details. ***A*** represents the vector along the $[10\bar{1}]$ direction. (**B**) A top view schematic diagram of the general crystal orientation in relation to the tensile stress along the meniscus direction. (**C**) Schmid factor profile as a function of θ for the nine slip systems, as numbered in (**A**).

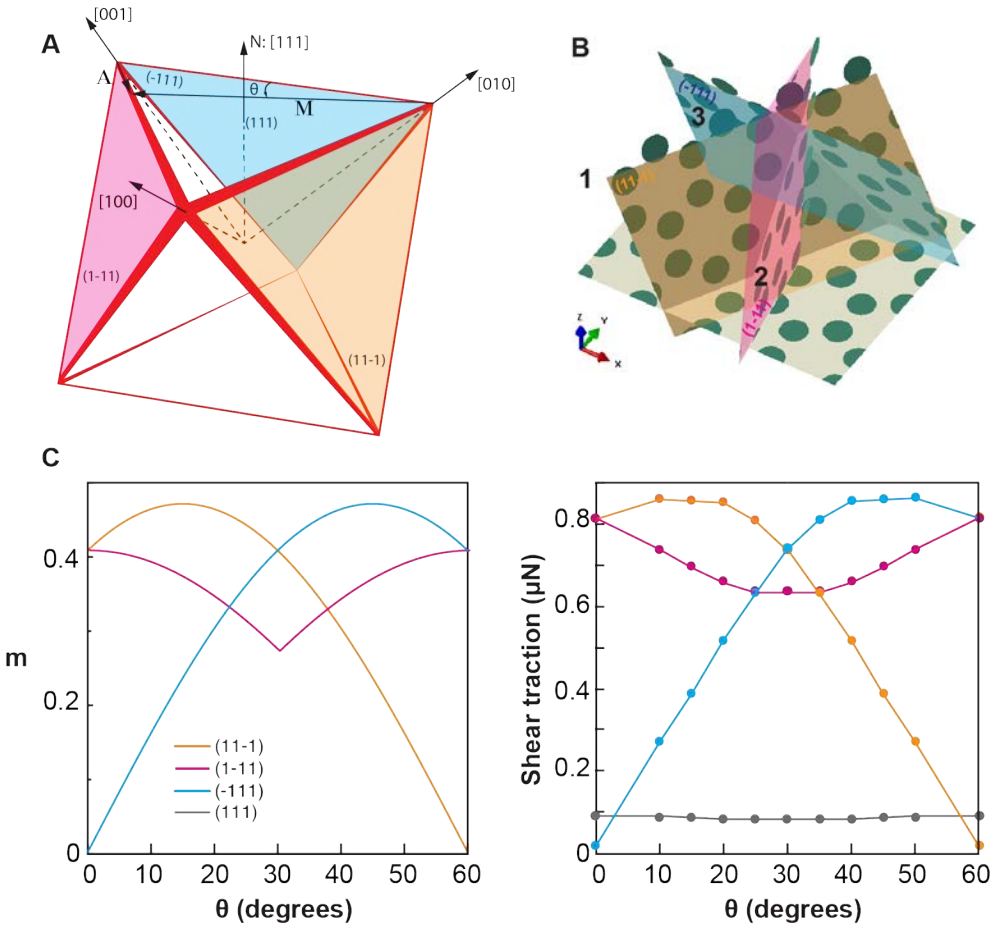

Fig. S11. Comparison between the Schmid factor analysis and the finite element simulation results. (**A**) Definition of the three slip planes $(11\bar{1})$, $(1\bar{1}1)$, and $(\bar{1}11)$ and (**B**) their correspondents in the representative volume used in the finite element simulation. (**C**) Schmid factor as a function of θ for the three slip planes and (**D**) the shear tractions on the slip planes from the simulation.

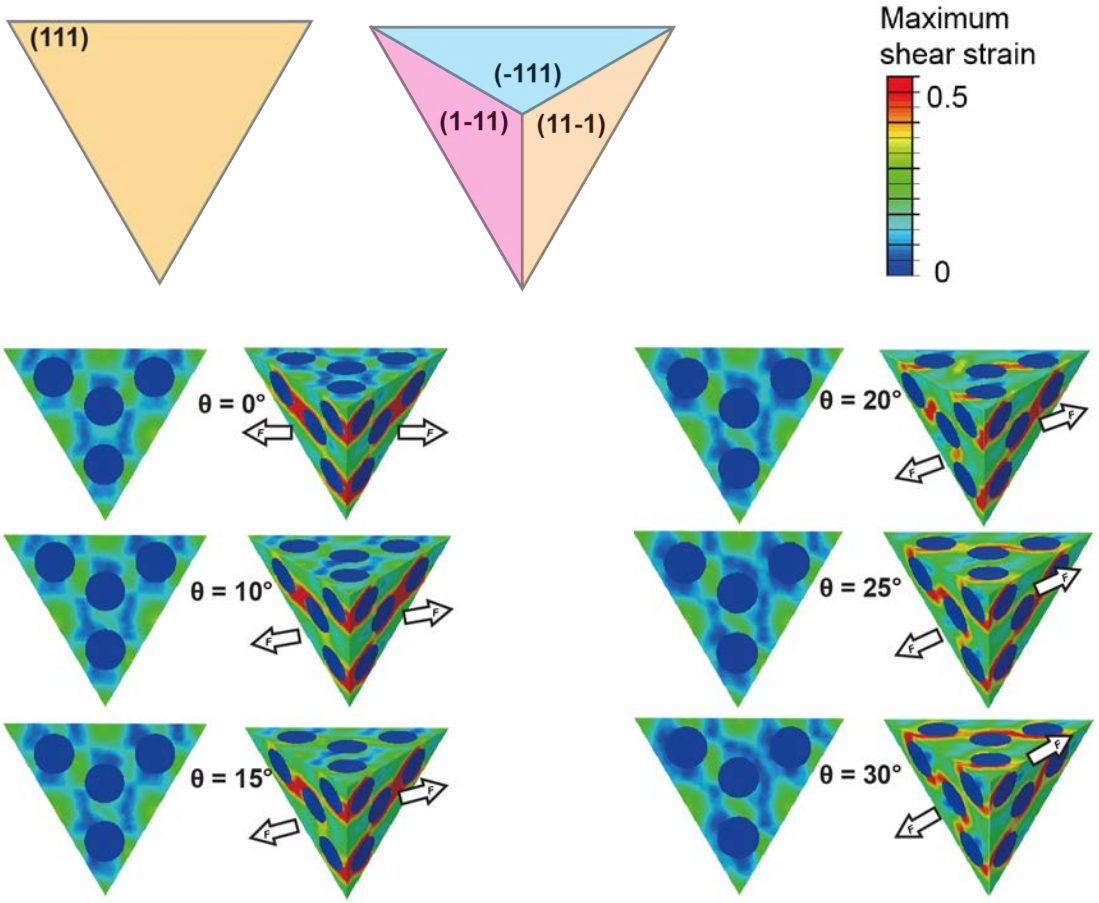

Fig. S12. **The distribution of shear deformation at different slip planes for different loading directions.** The contours of shear strain at different θs (the angle between the direction of stretch and the $[0\bar{1}1]$ direction) are presented on tetrahedra enclosed by planes (111), $(11\bar{1})$, $(1\bar{1}1)$, and $(\bar{1}11)$ described in Fig. S10(B). The strain contours present that the mismatch of shear strains between the $(11\bar{1})$, $(1\bar{1}1)$, and $(\bar{1}11)$ planes reach a maximum at 15° and achieves a minimum at 30°, which is consistent with the values of the Schmid factor in Fig. S10(C). The contours also suggest that dislocations will be most easily formed at θ = 15° on the $(11\bar{1})$ plane, where the shear deformation is most signification. In addition, the strain inbalance increases when θ deviates from 30°, suggesting that θ = 30° is a more stable status which might be related to the rotation of the crystal orientation.

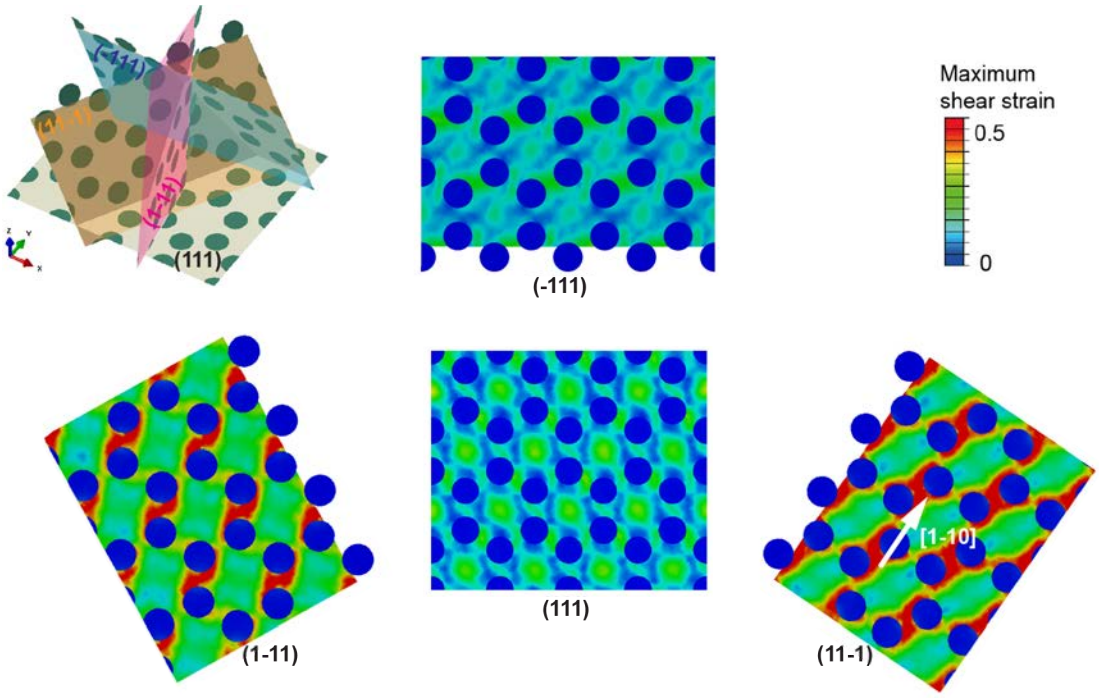

Fig. S13. **The shear strain contours at crystal orientation $\theta = 15°$** (θ is the angle between the direction of stretch and the $[0\bar{1}1]$ direction). Perpendicular views of the shear strain contours of slip planes (111), $(11\bar{1})$, $(1\bar{1}1)$, and $(\bar{1}11)$. The shear deformation is most signification on the $(11\bar{1})$ plane along the $[1\bar{1}0]$ direction marked by the white arrow. Dislocations and packing fault tend to form along this direction. Note that the contours are presented on the planes between the two closely packed particle layers, which have the maximum volume fraction of the matrix.

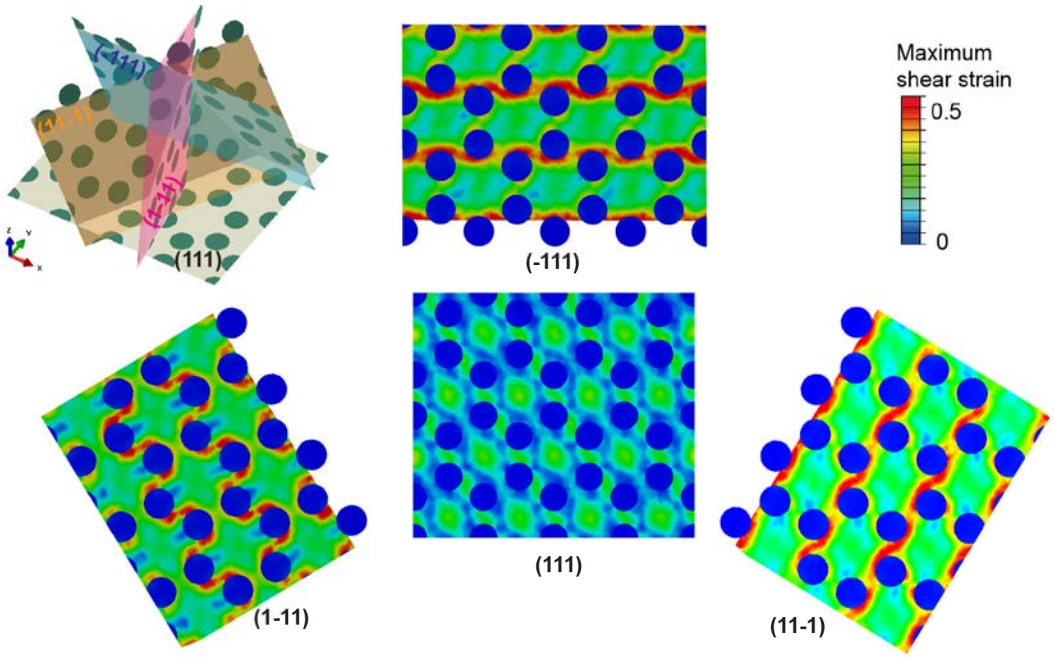

Fig. S14. **The shear strain contours at crystal orientations $\theta = 30°$** (the angle between the direction of stretch and the $[0\bar{1}1]$ direction). Perpendicular pictures of the shear strain contours on slip planes (111), $(11\bar{1})$, $(1\bar{1}1)$, and $(\bar{1}11)$. The $(11\bar{1})$, $(1\bar{1}1)$, and $(\bar{1}11)$ planes exhibit a similar level of shear strain. The shear strain is less significant than that of $\theta = 15°$ and all other crystal orientations.

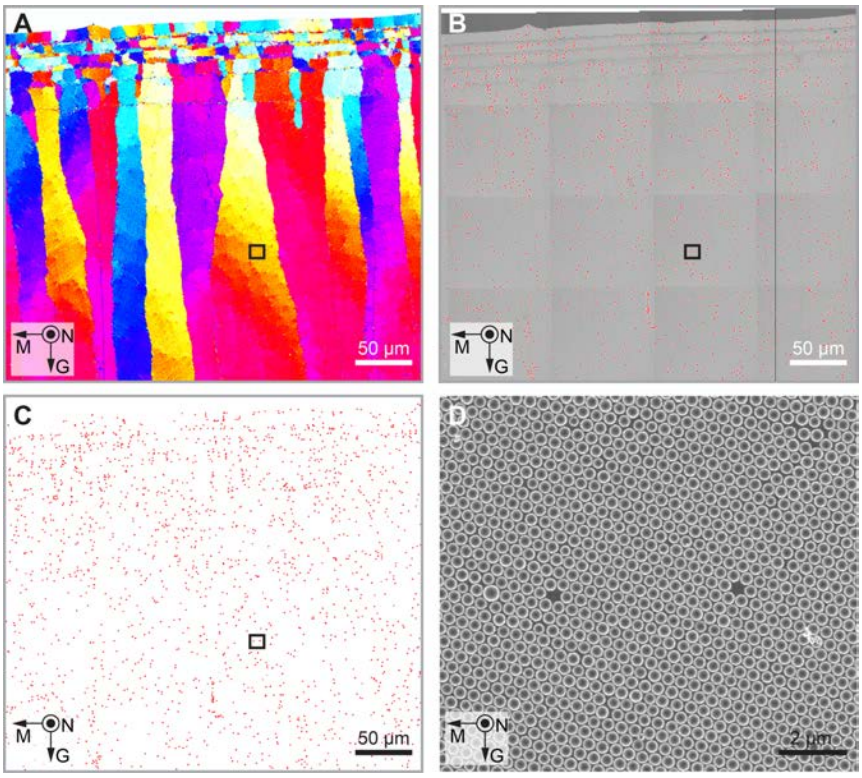

Fig. S15. Distributions of vacancy defects on the top layer of colloidal crystals. (**A**) Original orientation map and (**B,C**) corresponding distribution of vacancies (red dots). (**B**) represents the overlay of the original SEM image and location of vancances. (**D**) A high-magnification SEM of two representative vacancies. The position of this region is highlighted by the black boxes in (A-C).

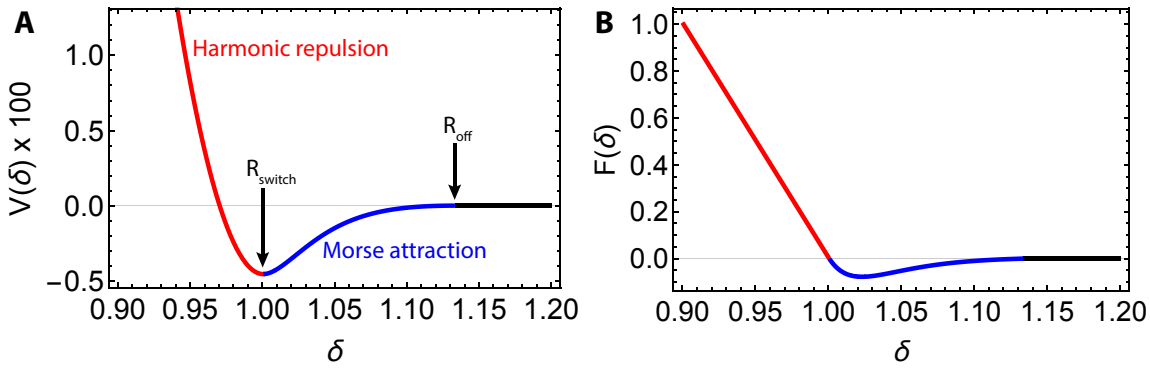

Fig. S16. Colloid-colloid interactions used in the numerical simulations. (**A**) Potential ($\boldsymbol{V(\delta)}$) between two adjacent colloidal particles as a function of inter-particle distance ($\boldsymbol{\delta}$). (**B**) Force ($\boldsymbol{F(\delta)}$) between two adjacent colloidal particles as a function of inter-particle distance ($\boldsymbol{\delta}$).

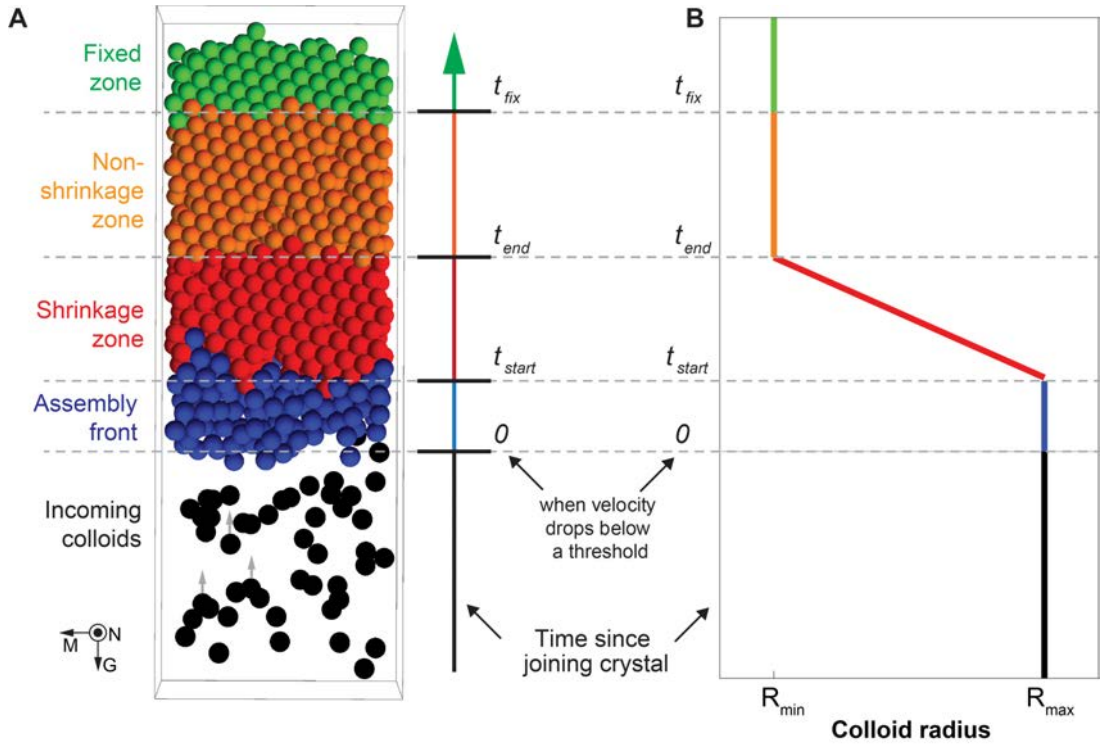

Fig. S17. Schematic illustration of the numerical simulations for colloidal crystallization. (**A**) Multiple zones exist in the assembly front: the colloidal particles are driven to the assembly front by the evaporation-induced fluid flow and join the assembly front, at which the time is set as 0. Once the particle velocity drops below a threshold at the assembly front, the particles will start shrinking their sizes between t_{start} and t_{end}. The particles are allowed to continue to move in positions after t_{end} and will be fixed at t_{fix}. (**B**) shows the radius profile of the colloidal particles at different zones.

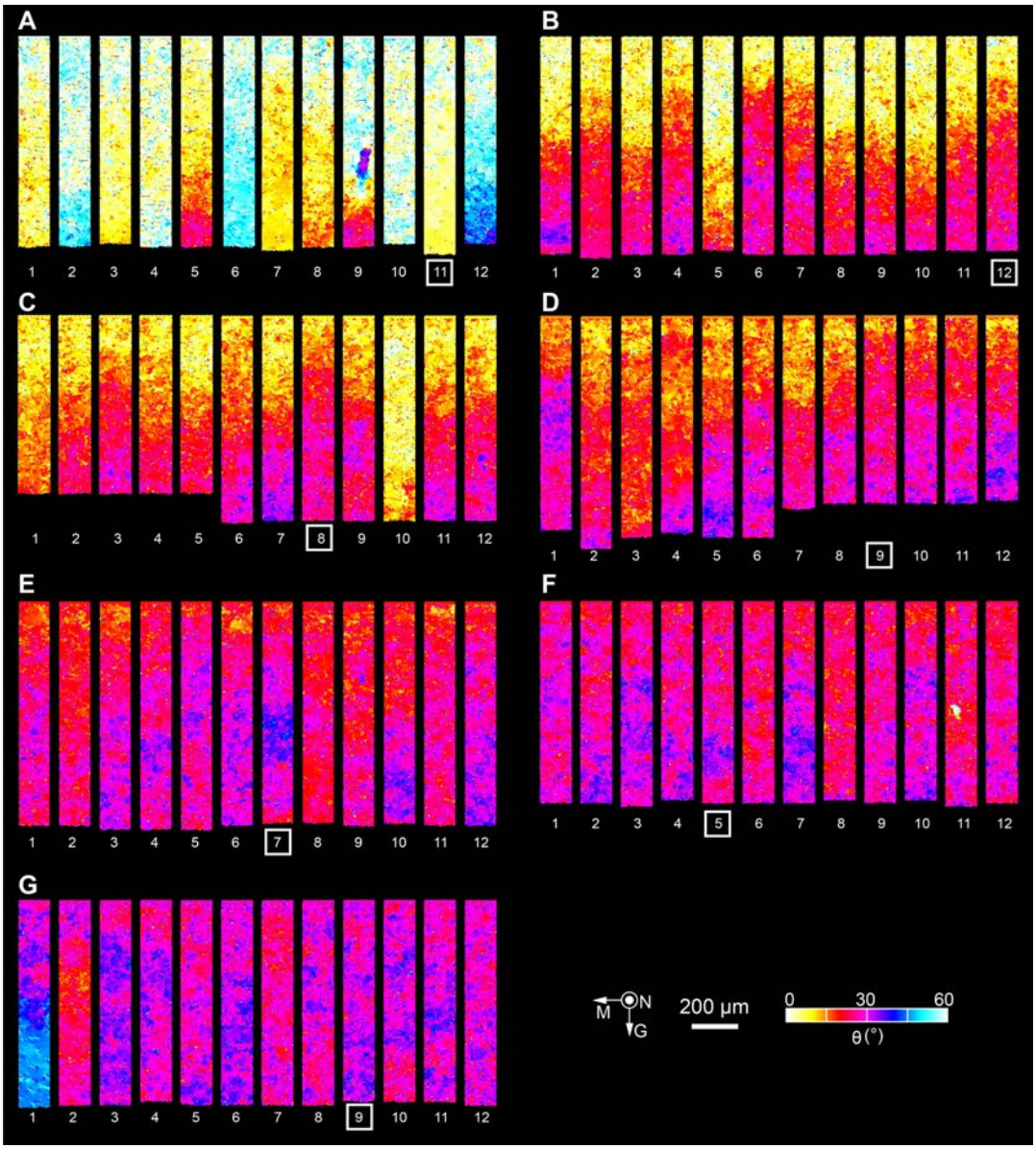

Fig. S18. Evaluation of the initial crystal orientation ($\boldsymbol{\theta_{initial}}$) on the crystallographic rotation during the assembly process. (A) $\boldsymbol{\theta_{initial} = 0°}$, (B), $\boldsymbol{\theta_{initial} = 5°}$, (C) $\boldsymbol{\theta_{initial} = 10°}$, (D) $\boldsymbol{\theta_{initial} = 15°}$, (E) $\boldsymbol{\theta_{initial} = 20°}$, (F) $\boldsymbol{\theta_{initial} = 25°}$, and (G) $\boldsymbol{\theta_{initial} = 30°}$. Note that multiple simulations are conducted to evaluate the statistical variations in each scenario. The simulations highlighted in the white boxes are selected for generating representative movies.

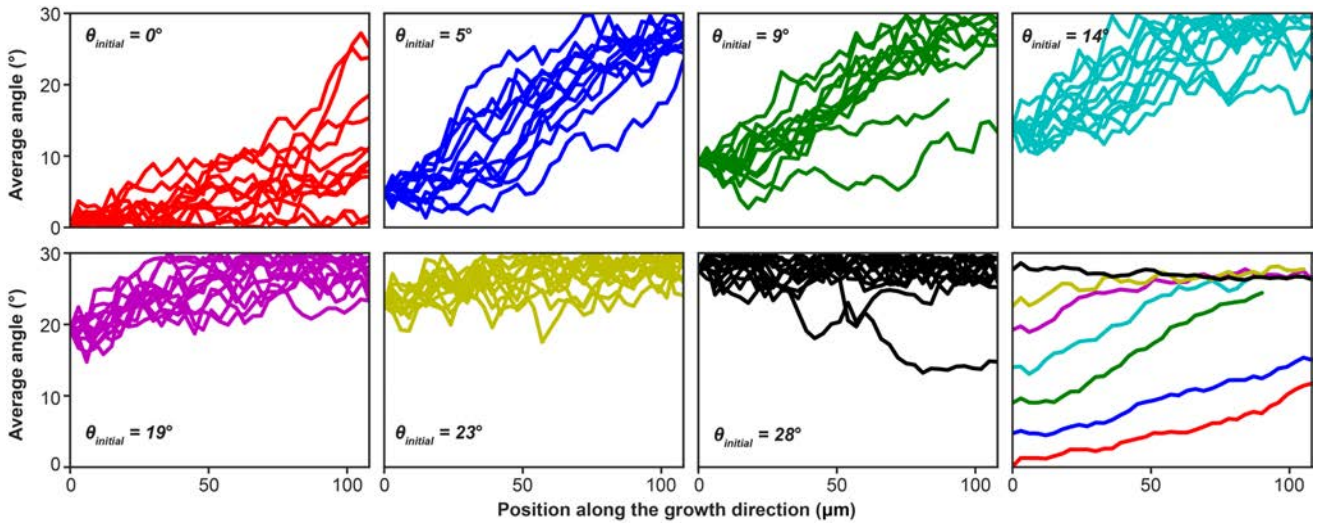

Fig. S19. Summary of crystal orientation profiles as a function of positions along the growth direction for the simulations shown in Fig. S18, illustrating the effects of initial crystal orientation. The last plot compares representative profiles from each case.

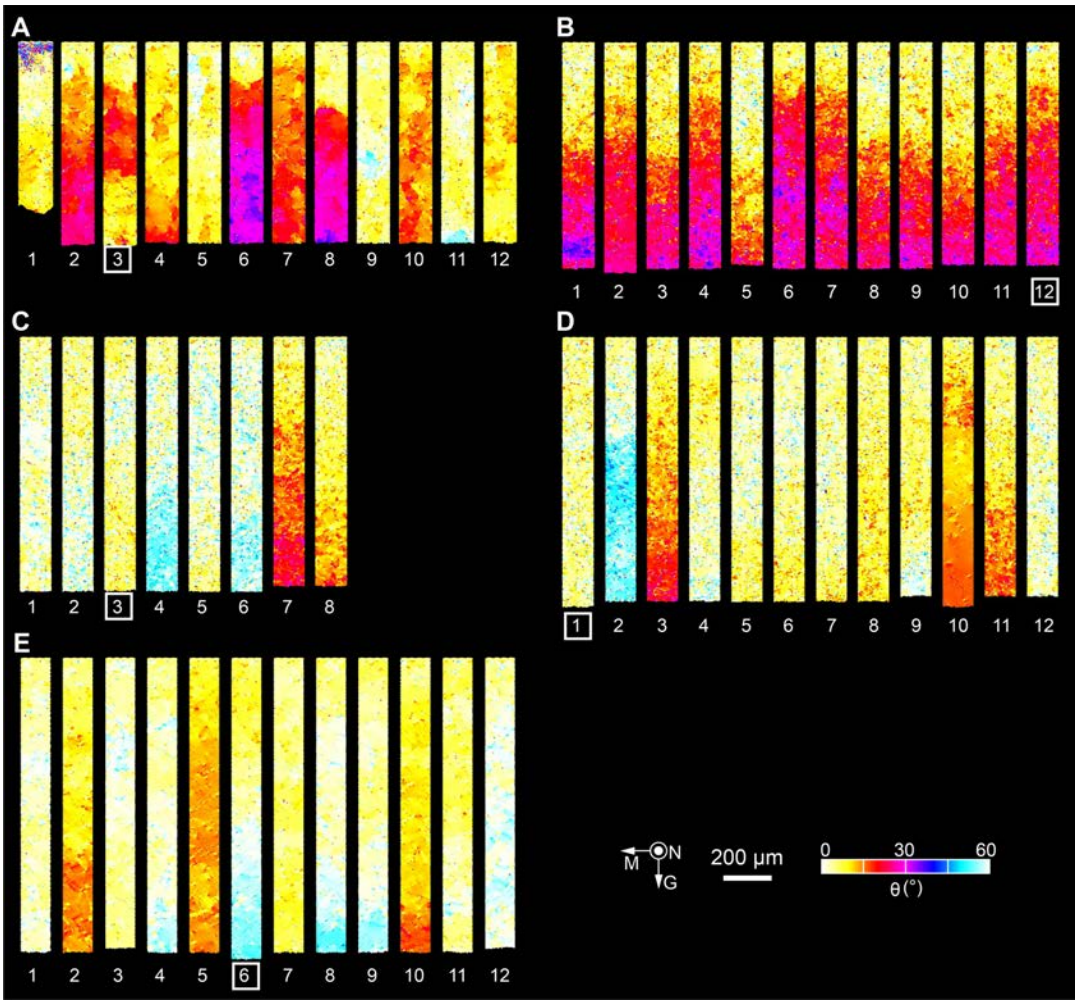

Fig. S20. Evaulation of particle shrinkage ($s = 1 - R_{min}/R_{max}$) on the crystallographic rotation during the assembly process. (**A**) s = 10%, (**B**), s = 5%, (**C**) s = 3%, (**D**) s = 2%, and s = 0. Note that multiple simulations are conducted to evaluate the statistical variations in each scenario. The simulations highlighted in the white boxes are selected for generating representative movies.

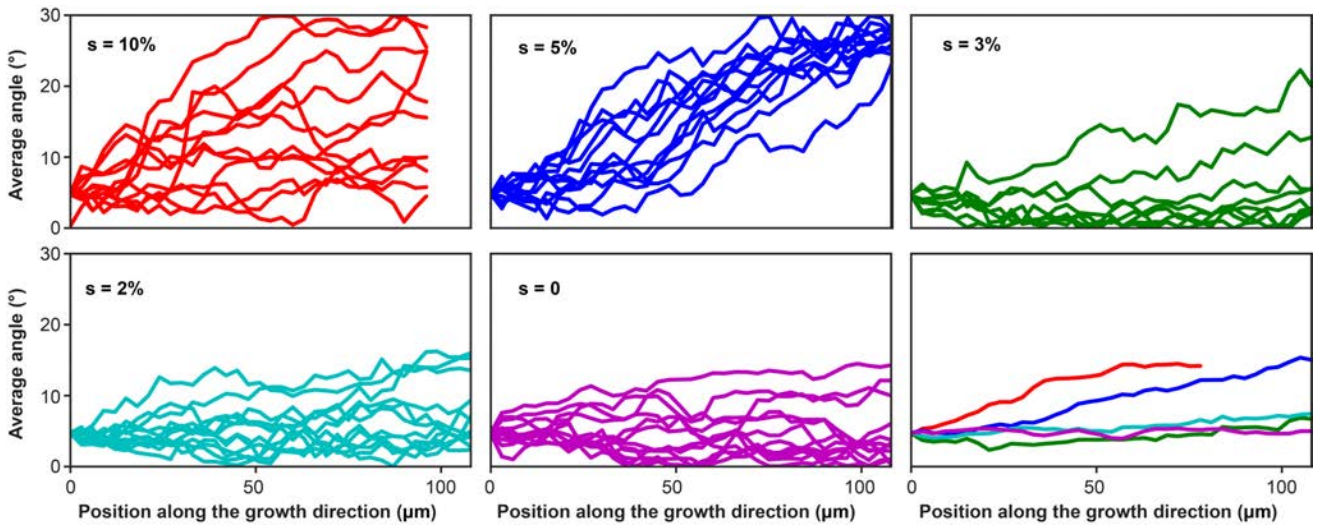

Fig. S21. Summary of crystal orientation profiles as a function of positions along the growth direction for the simulations shown in Fig. S20, illustrating the effects of particle shrinkage (*s*). The last plot compares representative profiles from each case.

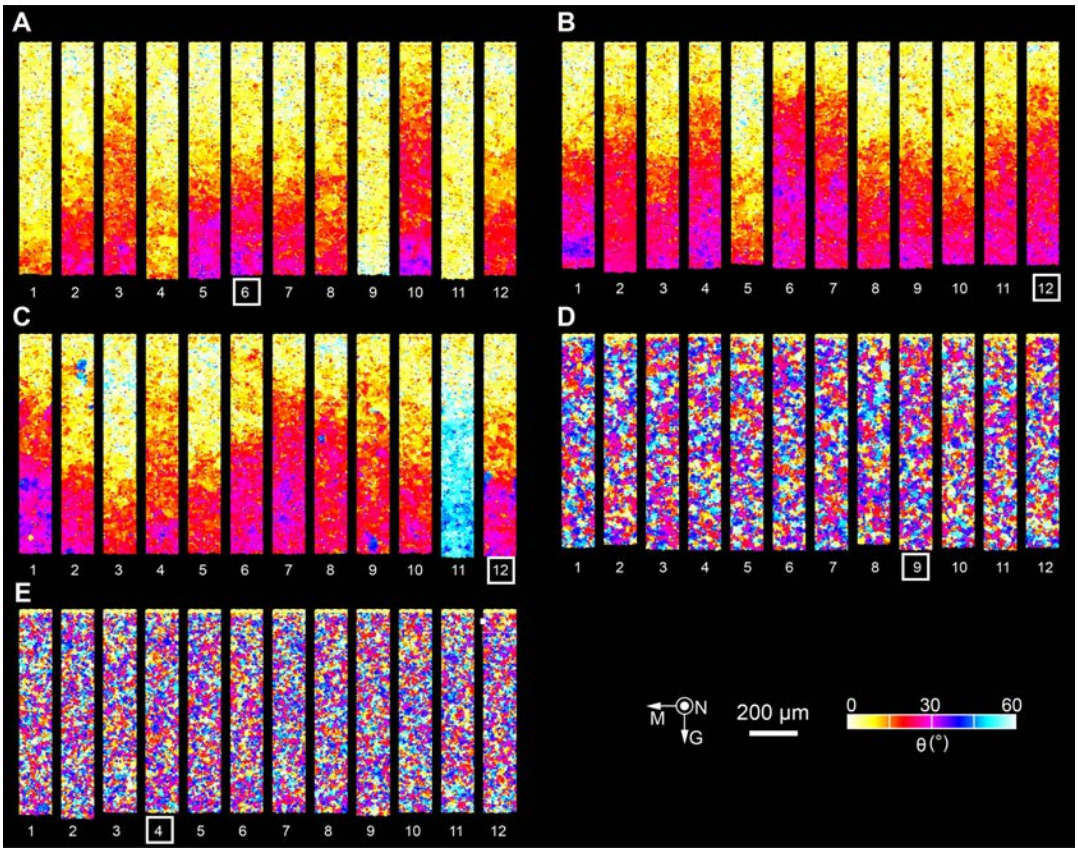

Fig. S22. Evaulation of particle size polydispersity (P) on the crystallographic rotation during the assembly process. (**A**) P = 0, (**B**), P = 0.028, (**C**) P = 0.050, (**D**) P = 0.100, and (**E**) P = 0.150. Note that multiple simulations are conducted to evaluate the statistical variations in each scenario. The simulations highlighted in the white boxes are selected for generating representative movies.

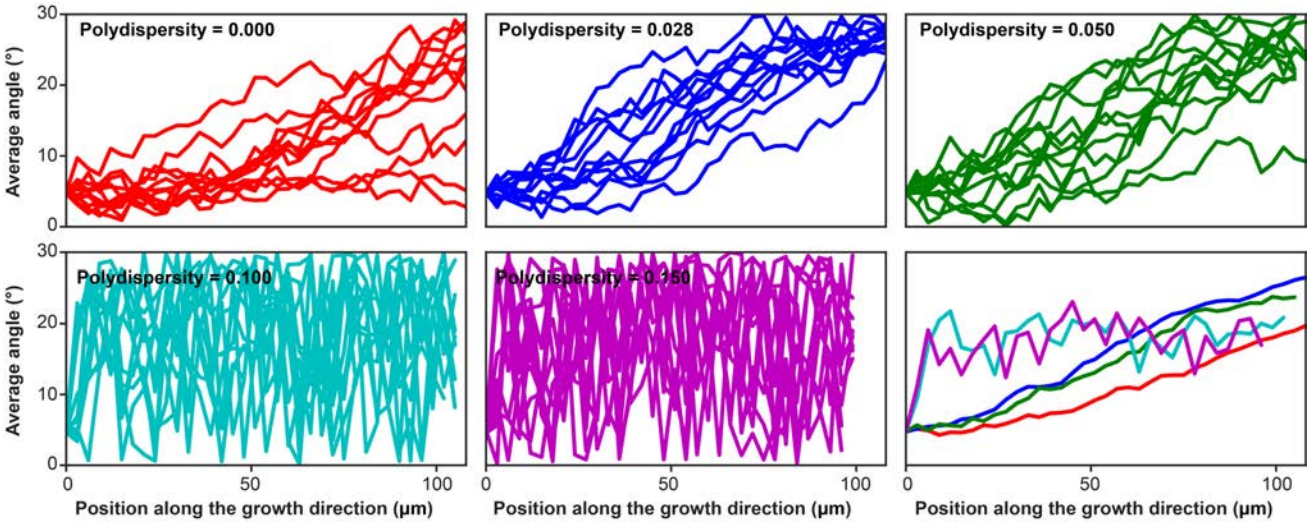

Fig. S23. Summary of crystal orientation profiles as a function of positions along the growth direction for the simulations shown in Fig. S2, illustrating the effects of particle size polydispersity. The last plot compares representative profiles from each case.

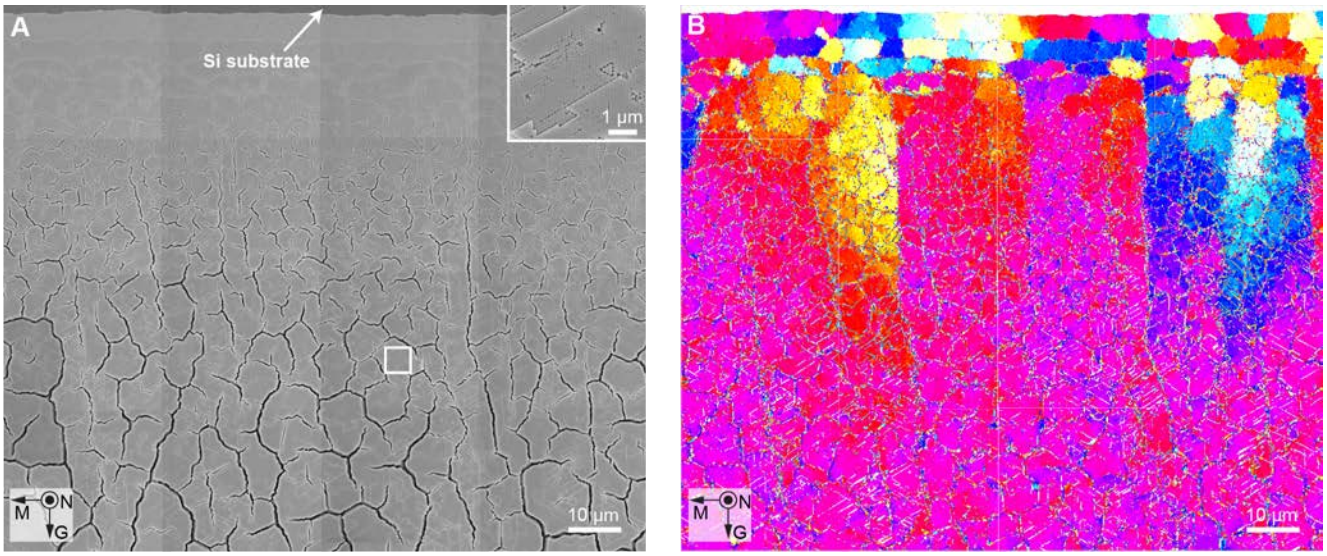

Fig. S24. Evolution of crystallographic orientation in the direct assembly of PS microparticles (size, 134 ± 5 nm). (**A**) A large-area stitched SEM image of the assembly taken from the growth front, where the Si substrate is indicated. The magnified view of the white boxed region is shown in the inset. (**B**) Corresponding original orientation map. Note the color scale is consistent with the rest of the paper.

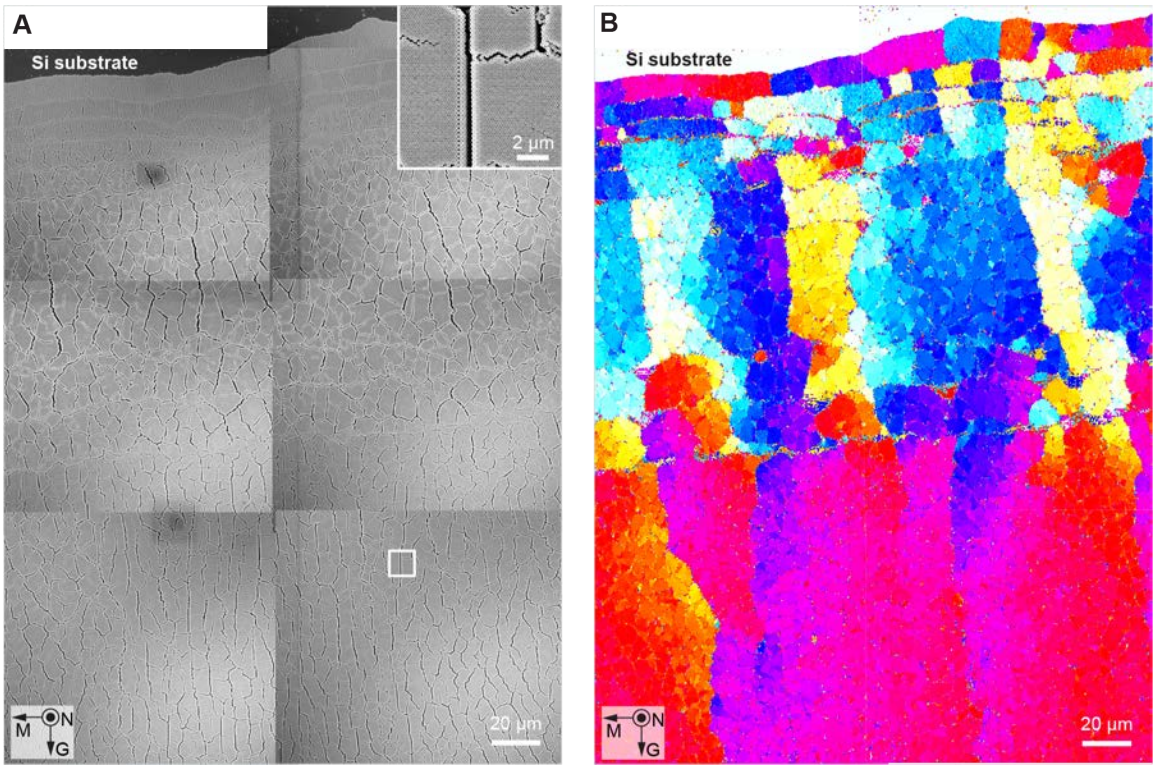

Fig. S25. Evolution of crystallographic orientation in the direct assembly of PS microparticles (size, 277 ± 14 nm). (**A**) A large-area stitched SEM image of the assembly taken from the growth front, where the Si substrate is indicated. The magnified view of the white boxed region is shown in the inset. (**B**) Corresponding original orientation map. Note the color scale is consistent with the rest of the paper.

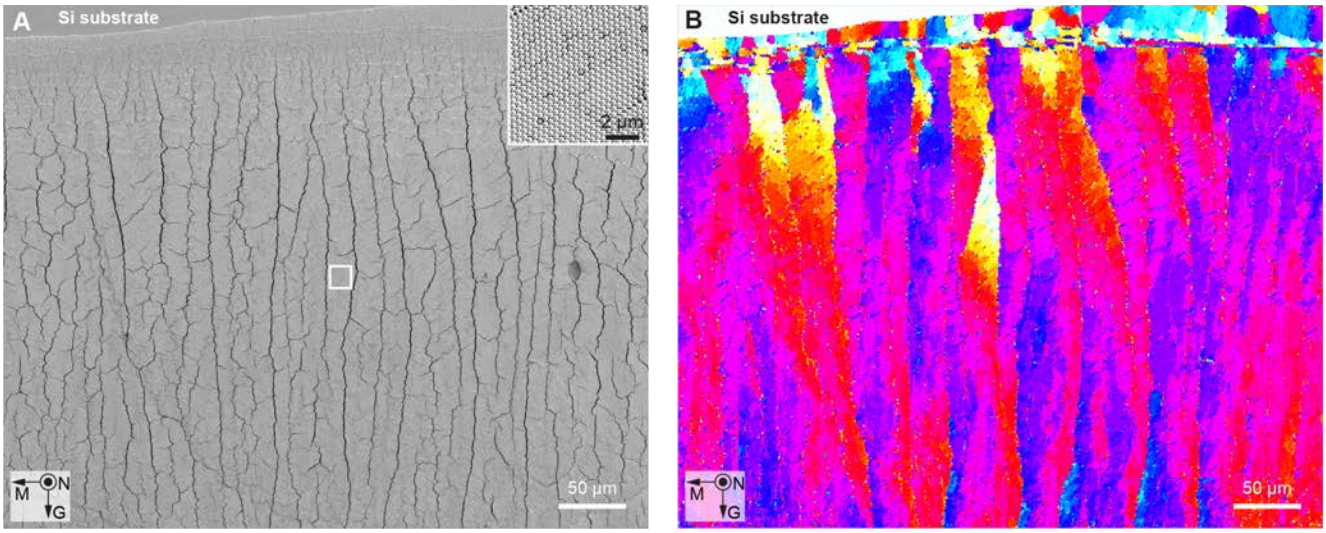

Fig. S26. Evolution of crystallographic orientation in the direct assembly of PS microparticles (size, 375 ± 11 nm). (**A**) A large-area stitched SEM image of the assembly taken from the growth front, where the Si substrate is indicated. The magnified view of the white boxed region is shown in the inset. (**B**) Corresponding original orientation map. Note the color scale is consistent with the rest of the paper.

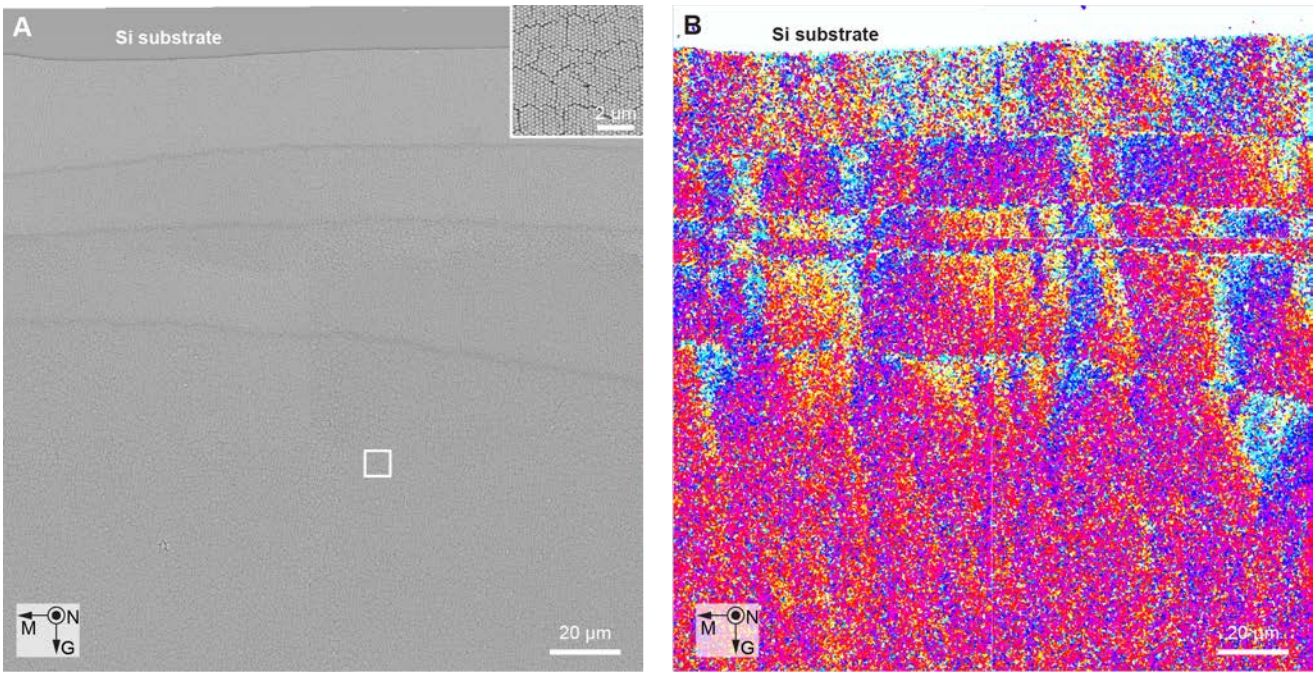

Fig. S27. Evolution of crystallographic orientation in the direct assembly of silica microparticles (209 ± 17 nm). (**A**) A large-area stitched SEM image of the assembly taken from the growth front, where the Si substrate is indicated. The magnified view of the white boxed region is shown in the inset. (**B**) Corresponding original orientation map. Note the color scale is consistent with the rest of the paper.

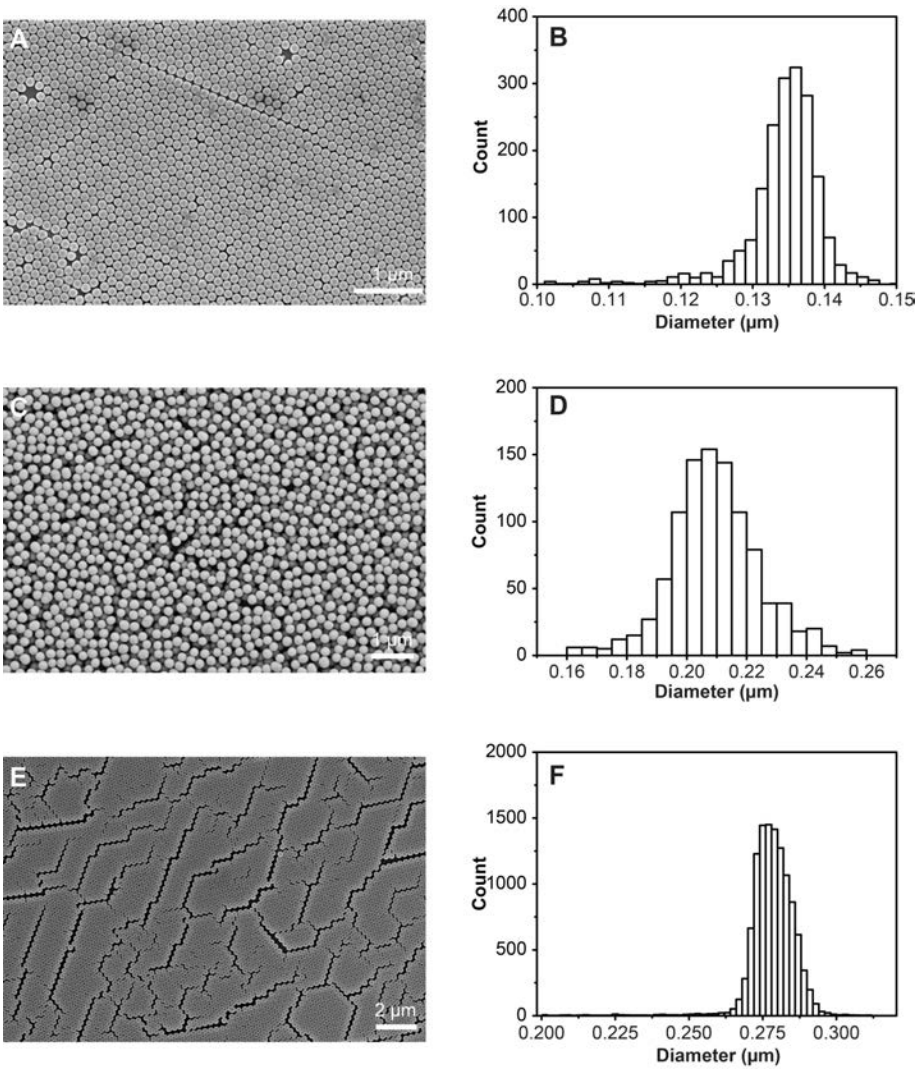

Fig. S28. Particle size measurement results. (**A,B**) PS particles: 134 ± 5 nm. (**C,D**) Silica particles: 209 ± 17 nm. (**E,F**) PS particles: 277 ± 14 nm. The bin width was chosen based on ref. 64.

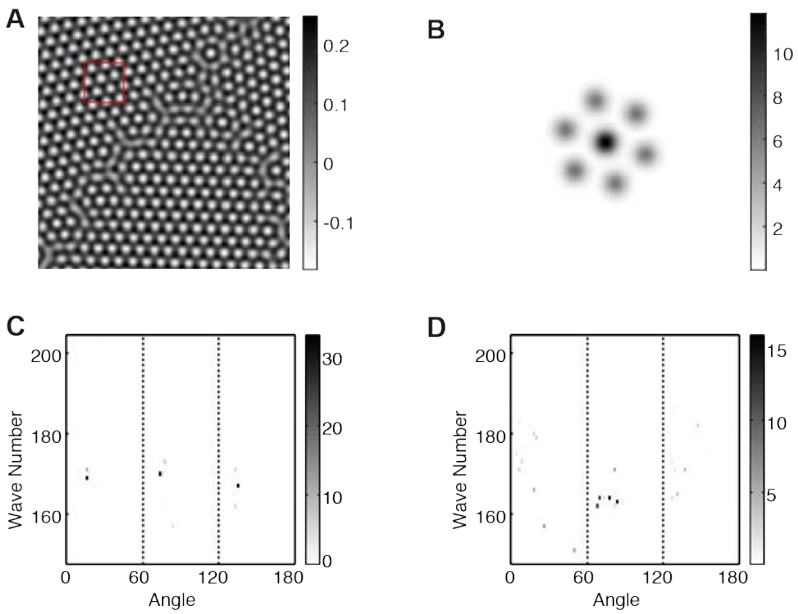

Fig. S29. Illustration of the synchrosqueezed transform technique for quantitative 2D crystallographic analysis. (**A**) An example of a crystal image. (**B**) The magnitude of the windowed Fourier transform at a local patch indicated by the red rectangle in (**A**). (**C**) The synchrosqueezed transform in polar coordinates at a point outside the defect region. Due to the symmetry of the Bravais lattice, only the result in the angle coordinate from 0 to 180 degrees is enough for image analysis. (**D**) The synchrosqueezed transform in polar coordinates at a point on the grain boundary.

List of supplementary movies:

Movie S1.
A representative modeling of colloidal assembly. The parameters used for this modeling include the intitial crystallographic angle $\theta = 5°$, average particle size d = 0.38 μm, size polydispersity P = 2.8%, and particle shrinkage s = 5%. The width of the simulation model is 124 μm.

Movie S2.
Effects of initial crystallographic orientation. The parameters used for this modeling include average particle size d = 0.38 μm, size polydispersity P = 2.8%, and particle shrinkage s = 5%. The intitial crystallographic angle θ is varied: $\theta = 0°$, 5°, 10°, 15°, 20°, 25°, and 30°. The width of the simulation model is 124 μm.

Movie S3.
Effects of particle size shrinkage. The parameters used for this modeling include the intitial crystallographic angle $\theta = 5°$, average particle size d = 0.38 μm, and size polydispersity P = 2.8%. The particle shrinkage s is varied: s = 10%, 5%, 3%, 2%, and 0. The width of the simulation model is 124 μm.

Movie S4.
Effects of particle size polydispersity. The parameters used for this modeling include the intitial crystallographic angle $\theta = 5°$, average particle size d = 0.38 μm, and particle shrinkage s = 5%. The size polydispersity P is varied: P = 0%, 2.8%, 5%, 10%, and 15%. The width of the simulation model is 124 μm.

References

1. V. N. Manoharan, Colloidal matter: Packing, geometry, and entropy. *Science* **349**, 1253751-1253751 (2015). doi:10.1126/science.1253751
2. Y. A. Vlasov, X.-Z. Bo, J. C. Sturm, D. J. Norris, On-chip natural assembly of silicon photonic bandgap crystals. *Nature* **414**, 289-293 (2001). doi:10.1038/35104529
3. B. Hatton, L. Mishchenko, S. Davis, K. H. Sandhage, J. Aizenberg, Assembly of large-area, highly ordered, crack-free inverse opal films. *Proc. Natl. Acad. Sci.* **107**, 10354-10359 (2010). doi:10.1073/pnas.1000954107
4. N. Vogel, M. Retsch, C.-A. Fustin, A. del Campo, U. Jonas, Advances in Colloidal Assembly: The Design of Structure and Hierarchy in Two and Three Dimensions. *Chem. Rev.* **115**, 6265-6311 (2015). doi:10.1021/cr400081d
5. K. R. Phillips, G. T. England, S. Sunny, E. Shirman, T. Shirman, N. Vogel, J. Aizenberg, A colloidoscope of colloid-based porous materials and their uses. *Chem. Soc. Rev.* **45**, 281-322 (2016). doi:10.1039/C5CS00533G
6. I. B. Burgess, N. Koay, K. P. Raymond, M. Kolle, M. Lončar, J. Aizenberg, Wetting in color: Colorimetric differentiation of organic liquids with high selectivity. *ACS Nano* **6**, 1427–1437 (2012). doi:10.1021/nn204220c
7. E. Shirman, T. Shirman, A. V. Shneidman, A. Grinthal, K. R. Phillips, H. Whelan, E. Bulger, M. Abramovitch, J. Patil, R. Nevarez, J. Aizenberg. Nevarez, Modular design of advanced catalytic materials using hybrid organic–inorganic raspberry particles. *Adv. Funct. Mater.* **28**, 1704559 (2018). doi:10.1002/adfm.201704559
8. I. B. Burgess, N. Koay, K. P. Raymond, M. Kolle, M. Lončar, J. Aizenberg, Wetting in color: colorimetric differentiation of organic liquids with high selectivity. *ACS nano* **6**, 1427-1437 (2012). doi:10.1021/nn204220c
9. P. Schall, I. Cohen, D. A. Weitz, F. Spaepen, Visualization of Dislocation Dynamics in Colloidal Crystals. *Science* **305**, 1944-1948 (2004). doi:10.1126/science.1102186
10. P. Schall, I. Cohen, D. A. Weitz, F. Spaepen, Visualizing dislocation nucleation by indenting colloidal crystals. *Nature* **440**, 319-323 (2006). doi:10.1038/nature04557
11. N. Y. C. Lin, M. Bierbaum, P. Schall, J. P. Sethna, I. Cohen, Measuring nonlinear stresses generated by defects in 3D colloidal crystals. *Nat. Mater.* **15**, 1172-1176 (2016). doi:10.1038/nmat4715
12. A. M. Alsayed, M. F. Islam, J. Zhang, P. J. Collings, A. G. Yodh, Premelting at Defects Within Bulk Colloidal Crystals. *Science* **309**, 1207-1210 (2005). doi:10.1126/science.1112399
13. R. Ganapathy, M. R. Buckley, S. J. Gerbode, I. Cohen, Direct Measurements of Island Growth and Step-Edge Barriers in Colloidal Epitaxy. *Science* **327**, 445-448 (2010). doi:10.1126/science.1179947
14. S. Suresh, Crystal deformation: Colloid model for atoms. *Nat. Mater.* **5**, 253-254 (2006). doi:10.1038/nmat1621
15. L. Mishchenko, B. Hatton, M. Kolle, J. Aizenberg, Patterning Hierarchy in Direct and Inverse Opal

Crystals. *Small* **8**, 1904-1911 (2012). doi:10.1002/smll.201102691

16. P. Born, S. Blum, A. Munoz, T. Kraus, Role of the Meniscus Shape in Large-Area Convective Particle Assembly. *Langmuir* **27**, 8621-8633 (2011). doi:10.1021/la2006138
17. D. J. Norris, E. G. Arlinghaus, L. Meng, R. Heiny, L. E. Scriven, Opaline Photonic Crystals: How Does Self-Assembly Work? *Adv. Mater.* **16**, 1393-1399 (2004). doi:10.1002/adma.200400455
18. A. L. Weldon, Investigations into Convective Deposition from Fundamental and Application-Driven Perspectives. (Lehigh University, Bethlehem, 2014).
19. N. Denkov, O. Velev, P. Kralchevsky, I. Ivanov, H. Yoshimura, K. Nagayama, Two-dimensional crystallization. *Nature* **361**, 26-26 (1993). doi:/10.1038/361026a0
20. N. Denkov, O. Velev, P. Kralchevski, I. Ivanov, H. Yoshimura, K. Nagayama, Mechanism of formation of two-dimensional crystals from latex particles on substrates. *Langmuir* **8**, 3183-3190 (1992). doi:10.1021/la00048a054
21. L. Pekurovsky, L. Scriven, On Capillary Forces and Stress in Drying Latex Coating. in Film Formation in Coatings: Mechanisms, Properties, and Morphology, American Chemical Society, Washington, DC, July 26, 2001. (eds. Provder, T. & Urban, M. W.) 27-40 (ACS Publications, 2001). doi:10.1021/bk-2001-0790.ch002
22. D. D. Brewer, J. Allen, M. R. Miller, J. M. de Santos, S. Kumar, D. J. Norris, M. Tsapatsis, L. E. Scriven, Mechanistic Principles of Colloidal Crystal Growth by Evaporation-Induced Convective Steering. *Langmuir* **24**, 13683-13693 (2008). doi:10.1021/la802180d
23. In this paper we use the standard crystallographic notation for the face-centered cubic system. The conventional coordinate axes are parallel to the 4-fold rotation axes, with length unit $a = \sigma\sqrt{2}$, where σ is the nearest-neighbor distance. [*hkl*] represents a direction in the crystal defined by a vector $\boldsymbol{r}_{hkl} = a(h,k,l)$, $\bar{h}$ means $-h$. (*hkl*) represents an infinite set of parallel planes perpendicular to $\boldsymbol{r}_{hkl}$, evenly spaced by $a^2/\boldsymbol{r}_{hkl}$. {*hkl*} and <*hkl*>, respectively, refer to the set of all (*hkl*) planes or [*hkl*] directions that are equivalent by crystal symmetry. A general treatment can be found for exame in M.J. Buerger, Elementary Crystallography, New York: Wiley (1956).
24. P. Born, A. Munoz, C. Cavelius, T. Kraus, Crystallization Mechanisms in Convective Particle Assembly. *Langmuir* **28**, 8300-8308 (2012). doi:10.1007/978-3-319-00230-9_3
25. M. Ishii, M. Harada, H. Nakamura, In situ observations of the self-assembling process of colloidal crystalline arrays. *Soft Matter* **3**, 872-876 (2007). doi:10.1039/B614593K
26. A. S. Dimitrov, K. Nagayama, Continuous Convective Assembling of Fine Particles into Two-Dimensional Arrays on Solid Surfaces. *Langmuir* **12**, 1303-1311 (1996). doi:10.1021/la9502251
27. H.-L. Li, W. Dong, H.-J. Bongard, F. Marlow, Improved Controllability of Opal Film Growth Using Capillaries for the Deposition Process. *J. Phys. Chem. B* **109**, 9939-9945 (2005). doi:10.1021/jp050385d
28. K. Wostyn, Y. Zhao, B. Yee, K. Clays, A. Persoons, G. d. Schaetzen, L. Hellemans, Optical properties and orientation of arrays of polystyrene spheres deposited using convective self-assembly. *J. Chem. Phys.* **118**, 10752-10757 (2003). doi:10.1063/1.1573173
29. M. A. McLachlan, N. P. Johnson, R. M. De La Rue, D. W. McComb, Thin film photonic crystals: Synthesis and characterisation. *J. Mater. Chem.* **14**, 144-150 (2004). doi:10.1039/B310759K

30. M. A. McLachlan, N. P. Johnson, R. M. De La Rue, D. W. McComb, Domain size and thickness control of thin film photonic crystals. *J. Mater. Chem.* **15**, 369-371 (2005). doi:10.1039/B414874F

31. Á. G. Marín, H. Gelderblom, D. Lohse, J. H. Snoeijer, Order-to-disorder transition in ring-shaped colloidal stains. *Phys. Rev. Lett.* **107**, 085502 (2011). doi:10.1103/PhysRevLett.107.085502

32. S. Mann, Molecular tectonics in biomineralization and biomimetic materials chemistry. *Nature* **365**, 499-505 (1993). doi:10.1038/365499a0

33. S. Weiner, W. Traub, Mineral phases in biology - Macromolecules in mollusc shells and their functions in biomineralization. *Phil. Trans. R. Soc. Lond. B* **304**, 425–434 (1984). doi:10.1098/rstb.1984.0036

34. J. Aizenberg, A. J. Black, G. M. Whitesides, Control of crystal nucleation by patterned self-assembled monolayers. *Nature* **398**, 495–498 (1999). doi:10.1038/19047

35. A. Bastos, S. Zaefferer, D. Raabe, C. Schuh, Characterization of the microstructure and texture of nanostructured electrodeposited NiCo using electron backscatter diffraction (EBSD). *Acta Mater.* **54**, 2451-2462 (2006). doi:10.1016/j.actamat.2006.01.033

36. R. A. Knepper, *Thermomechanical behavior and microstructure evolution of tantalum thin films during the beta-alpha phase transformation* (Cornell University, 2007).

37. A. G. Checa, J. T. Bonarski, M. G. Willinger, M. Faryna, K. Berent, B. Kania, A. González-Segura, C. M. Pina, J. Pospiech, A. Morawiec, Crystallographic orientation inhomogeneity and crystal splitting in biogenic calcite. *J. R. Soc. Interface* **10**, (2013). doi:10.1098/rsif.2013.0425

38. P. V. Braun, S. A. Rinne, F. García-Santamaría, Introducing Defects in 3D Photonic Crystals: State of the Art. *Adv. Mater.* **18**, 2665-2678 (2006). doi:10.1002/adma.200600769

39. A. van Blaaderen, R. Ruel, P. Wiltzius, Template-directed colloidal crystallization. *Nature* **385**, 321-324 (1997). doi:10.1038/385321a0

40. W. T. M. Irvine, V. Vitelli, P. M. Chaikin, Pleats in crystals on curved surfaces. *Nature* **468**, 947–951 (2010). doi:10.1038/nature09620

41. J. Lu, B. Wirth, H. Yang, Combining 2D synchrosqueezed wave packet transform with optimization for crystal image analysis. *J. Mech. Phys. Solids* **89**, 194-210 (2016). doi:10.1016/j.jmps.2016.01.002

42. P. Pieranski, L. Strzelecki, B. Pansu, Thin Colloidal Crystals. *Phys. Rev. Lett.* **50**, 900-903 (1983). doi:10.1103/PhysRevLett.50.900

43. B. Pansu, P. Pieranski, P. Pieranski, Structures of thin layers of hard spheres: high pressure limit. *J. Phys. France* **45**, 331-339 (1984). doi:10.1051/jphys:01984004502033100

44. D. Hull, D. J. Bacon, *Introduction to dislocations* (Elsevier Science, 2001).

45. L. Goehring, A. Nakahara, T. Dutta, S. Tarafdar, S. Kitsunezaki, *Desiccation cracks and their patterns: formation and modelling in science and nature* (John Wiley & Sons, 2015).

46. J. Zhou, J. Wang, Y. Huang, G. Liu, L. Wang, S. Chen, X. Li, D. Wang, Y. Song, L. Jiang, Large-area crack-free single-crystal photonic crystals via combined effects of polymerization-assisted assembly and flexible substrate. *NPG Asia Mater.* **4**, e21-e21 (2012). doi:10.1038/am.2012.38

47. K. B. Singh, M. S. Tirumkudulu, Cracking in drying colloidal films. *Phys. Rev. Lett.* **98**, 218302 (2007). doi:10.1103/PhysRevLett.98.218302

48. Xu, P., Mujumdar, A. & Yu, B. Drying-induced cracks in thin film fabricated from colloidal dispersions. *Drying technology* **27**, 636-652 (2009). doi:10.1080/07373930902820804

49. K. R. Phillips, C. T. Zhang, T. Yang, T. Kay, C. Gao, S. Brandt, L. Liu, H. Yang, Y. Li, J. Aizenberg, L. Li, Fabrication of photonic microbricks via crack engineering of colloidal crystals. *Adv. Funct. Mater.* **30**, 1908242 (2019). doi:10.1002/adfm.201908242

50. W. F. Hosford, *Mechanical behavior of materials* (Cambridge University Press, 2010).

51. Y. Xu, G. K. German, A. F. Mertz, E. R. Dufresne, Imaging stress and strain in the fracture of drying colloidal films. *Soft Matter* **9**, 3735-3740 (2013). doi:10.1039/C3SM27912J

52. R. E. Reed-Hill, R. Abbaschian, R. Abbaschian, *Physical metallurgy principles*. (Van Nostrand, 1973).

53. J. F. Nye, Some geometrical relations in dislocated crystals. *Acta Metall.* **1**, 153-162 (1953). doi:10.1016/0001-6160(53)90054-6

54. A. Arsenlis, D. M. Parks, Crystallographic aspects of geometrically-necessary and statistically-stored dislocation density. *Acta Mater.* **47**, 1597-1611 (1999). doi:10.1016/S1359-6454(99)00020-8

55. S. Pronk, D. Frenkel, Can stacking faults in hard-sphere crystals anneal out spontaneously? *J. Chem. Phys.* **110**, 4589-4592 (1999). doi:10.1063/1.478339

56. J. Matthews, A. Blakeslee, Defects in epitaxial multilayers: I. Misfit dislocations. *J. Cryst. Growth* **27**, 118-125 (1974). doi:10.1016/S0022-0248(74)80055-2

57. J. Hirth, J. Lothe, *Theory of Dislocations*. (Krieger Publishing Company, 1992).

58. M. Jorand, F. Rothen, Dislocation motion in colloidal crystals. *Le Journal de Physique Colloques* **46**, C3-245-C243-255 (1985). doi:10.1051/jphyscol:1985319

59. O'Brien, M. N., Jones, M. R. & Mirkin, C. A. The nature and implications of uniformity in the hierarchical organization of nanomaterials. *Proceedings of the National Academy of Sciences* **113**, 11717-11725 (2016). doi:10.1073/pnas.1605289113

60. S. Auer, D. Frenkel, Prediction of absolute crystal-nucleation rate in hard-sphere colloids. *Nature* **409**, 1020-1023 (2001). doi:10.1038/35059035

61. E. R. Dufresne, D. J. Stark, N. A. Greenblatt, J. X. Cheng, J. W. Hutchinson, L. Mahadevan, D. A. Weitz, Dynamics of Fracture in Drying Suspensions. *Langmuir* **22**, 7144-7147 (2006). doi:10.1021/la061251+

62. E. Zolotoyabko, Anisotropic Lattice Distortions in Biogenic Minerals Originated from Strong Atomic Interactions at Organic/Inorganic Interfaces. *Adv. Mater. Interfaces* **4**, 1600189 (2017). doi:10.1002/admi.201700073

63. B. T. Holland, C. F. Blanford, T. Do, A. Stein, Synthesis of highly ordered, three-dimensional, macroporous structures of amorphous or crystalline inorganic oxides, phosphates, and hybrid composites. *Chem. Mater.* **11**, 795–805 (1999). doi:10.1021/cm980666g

64. J. Schindelin et al. Fiji: An open-source platform for biological-image analysis. *Nat. Methods* **9**, 676-682 (2012). doi:10.1038/nmeth.2019

65. D. W. Scott, On optimal and data-based histograms. *Biometrika* **66**, 605-610 (1979). doi:10.1093/BIOMET/66.3.605

66. J. C. Crocker, D. G. Grier, Methods of digital video microscopy for colloidal studies. *J. Colloid. Interface Sci.* **179**, 298-310 (1996). doi: 10.1006/jcis.1996.0217

67. H. Yang, L. Ying, Synchrosqueezed Wave Packet Transform for 2D Mode Decomposition. *SIAM J. Imaging Sci.* **6**, 1979-2009 (2013). doi:10.1137/120891113

68. H. Yang, L. Ying, Synchrosqueezed Curvelet Transform for Two-Dimensional Mode Decomposition. *SIAM J. Math. Anal.* **46**, 2052-2083 (2014). doi:10.1137/130939912

69. H. Yang, J. Lu, L. J. M. M. Ying, Crystal Image Analysis Using 2D Synchrosqueezed Transforms. *Multiscale Model. Simul.* **13**, 1542-1572 (2015). doi:10.1137/140955872